Chemical Science

Accepted Manuscript

This article can be cited before page numbers have been issued, to do this please use: X. Chen, C. Huang, J. Liu, Q. Xiang, L. Zhang, X. Huang, L. Li and Z. Wei, *Chem. Sci.*, 2026, DOI: 10.1039/D6SC03869G.

ROYAL SOCIETY OF CHEMISTRY

rsc.li/chemical-science

Dynamic Stability of OER Electrocatalysts in Water Electrolyzers: Multiscale Deactivation Mechanisms and Regulation Strategies

Xia Chen [a], Chengming Huang [a], Jin Liu [a], Qiong Xiang [a] , Ling Zhang [a]*, Xun Huang, Li Li [a]*, and Zidong Wei [a]

[a] Center of Advanced Electrochemical Energy (CAEE), Institute of Advanced Interdisciplinary Studies; State Key Laboratory of Advanced Chemical Power Sources, School of Chemistry and Chemical Engineering, Chongqing University, Chongqing, China

* Corresponding authors

E-mail addresses: liliracial@cqu.edu.cn

Abstract: Water electrolysis is widely acknowledged as a vital pathway for achieving deep decarbonization and facilitating large-scale integration of renewable energy sources. Nonetheless, the anodic oxygen evolution reaction (OER) presents a significant efficiency bottleneck due to its inherently sluggish kinetics associated with multi-electron and proton transfer. In addition to the necessity for high catalytic activity, the long-term stability of OER electrocatalysis has garnered increasing attention. This review focuses on stability under realistic conditions and on understanding and elucidating OER deactivation mechanisms at the microscopic, mesoscopic, and macroscopic levels. At the micro level, the analysis delves into the disruption of dynamic phase equilibrium, stoichiometric deviations caused by selective dissolution, and deactivation resulting from the lattice oxygen mechanism. On the meso scale, it examines the extent of surface reconstruction, the inadequacy of nanomechanical robustness, and catalyst-layer delamination prompted by ripening and agglomeration. At the macro level, it considers corrosion resulting from start-stop cycling, component degradation, and the effects of harsh operational environments. Furthermore, the review summarizes current strategies aimed at enhancing stability, emphasizing intrinsic stability design as a foundational element, supplemented by dynamic stability regulation and optimization of operational conditions. Collectively, these approaches facilitate sustained catalytic performance under high potentials and extended operational periods, paving the way for durable electrocatalytic systems. Lastly, future research should prioritize the stabilization of OER electrocatalysis and its scalable application in industrial water electrolysis.

Keywords： OER; stability; operating conditions; multi-scale deactivation; strategy

View Article Online
DOI: 10.1039/D6SC03869G

1. Introduction

Hydrogen, with its highest energy density, clean combustion product, and abundant sources, has long been heralded as the ideal energy carrier for the 21st century.[1-3] Consequently, developing a hydrogen-based sustainable energy system has become an important strategic pathway for countries around the world to address global climate change and advance carbon neutrality goals. Among the various technological approaches to large-scale hydrogen production, water electrolysis driven by renewable energy is especially noteworthy due to its potential for sustainable, low-emission hydrogen generation. However, the manufacturing costs of hydrogen using this advanced technology are high, at $4-6 USD/kg, which is significantly higher than the cost of hydrogen produced from fossil fuels and hinders its widespread application. According to U.S. Department of Energy (DOE) estimates, hydrogen manufactured through water electrolysis will become economically competitive with hydrogen from fossil fuels only when its production cost drops to $1 per kilogram. To meet this challenge, countries have formulated research and development plans for water electrolysis technology, setting clear technical targets. For example, the energy conversion efficiency of electrolyzer systems is required to reach 75% by 2050, with a service life target of 60,000 h.[4-6]

Electrochemical water splitting comprises a cathodic hydrogen evolution reaction (HER) and an anodic oxygen evolution reaction (OER). While cathodic catalysts have largely met the requirements for industrial implementation, the anode remains a major bottleneck. One of the most critical challenges impeding large-scale deployment is the insufficient long-term durability of OER electrocatalysts under practical operating conditions.[7, 8] Current research efforts have yielded significant breakthroughs in the development of OER electrocatalysts under laboratory conditions. In acidic media, IrO_2- and RuO_2-based catalysts have exhibited markedly enhanced activity at low to moderate current densities. [9, 10] For instance, iridium oxide delivers a low overpotential of 197 mV at 10 mA cm^{-2} and exhibits a high intrinsic reaction rate, as reflected by a large TOF at 1.50 V vs RHE.[11] Moreover, anhydrous highly crystalline RuO_2 exhibits markedly improved stability, enabling continuous operation for over 500 h at 1 A cm^{-2}.[12, 13] Meanwhile, alkaline media enable a broad range of non-precious-metal OER electrocatalysts, including transition-metal oxides and hydroxides, layered double hydroxides, and high-entropy oxides, with several systems showing improved activity and short-term stability at low current densities (≤10 mA cm^{-2}).[14-16] For example, Fe-

Co_3O_4 exhibited promising OER performance with the overpotential of 384 mV at 10 mA cm^{-2}, and no noticeable degradation could be found after constant operation of over 60 h.[17] In addition, introducing high-density cation vacancies to reinforce intrinsic structural robustness has enabled NiFe-based catalysts to operate stably for more than 900 h under constant current conditions with negligible potential drift, demonstrating a substantial enhancement in low-current stability.[18] It should be noted, however, that most of the above performance metrics were obtained under laboratory conditions. For industrial applications that demand higher current densities, lower cost, and longer lifetime, stability issues remain prominent and complex.

Overall, it should be emphasized that a substantial gap still exists between the testing conditions commonly employed in the laboratory and the realistic operating environment of industrial electrolyzers.[19, 20] Under industrially relevant operating conditions, catalysts experience severe structural reconstruction,[20] dissolution of active species,[21] corrosion of underlying substrates,[22] and mechanical delamination induced by vigorous oxygen bubble evolution,[23] leading to exponentially accelerated degradation and lifetimes far below the ≥10,000 hours required for commercial deployment.[24] As summarized in Table 1, in most experimental studies, catalysts are assessed at low current densities (10-100 mA cm^{-2}), typically using rotating disk electrodes (RDE) to mitigate mass-transport limitations and extract intrinsic activity metrics such as turnover frequency (TOF).[25, 26] In contrast, industrial electrolysis must operate at high current densities (>500 mA cm^{-2}) to reduce capital and operational costs.[27] Under such conditions, rapid gas evolution leads to bubble accumulation and thickened boundary layers, imposing severe mass-transport constraints.[28]

Moreover, laboratory tests are often conducted under steady-state operation, whereas real-world systems are frequently coupled with intermittent renewable energy sources. Catalysts must therefore withstand current pulsation, voltage fluctuations, and repeated start-stop cycles, all of which significantly impact durability.[29, 30] The challenges of industrial operation are further amplified by harsh environmental and temporal scales. Elevated temperatures, strongly corrosive electrolytes, and high oxidative potentials accelerate dissolution and structural degradation. Meanwhile, industrial operation requires lifetimes extending from hundreds to several thousand hours, during which slow deactivation pathways such as Ostwald ripening[31] and compositional migration become pronounced and ultimately govern long-term catalyst failure.[32] Therefore, stability tests should be rationally selected according to the targeted

View Article Online
DOI: 10.1039/D6SC03869G

industrial degradation scenarios. High-current-density chronopotentiometry under elevated temperatures is more suitable for assessing continuous operation stability, mass-transport limitations, bubble-induced stress, and interfacial degradation. Dynamic-load and start-stop cycling tests are more relevant for evaluating catalyst dissolution, redox-driven structural changes, and mechanical detachment caused by intermittent renewable electricity input. In comparison with short-term low-current-density measurements, long-term tests performed at industrially relevant current densities, temperatures, electrolyte concentrations, and electrode configurations provide more meaningful information for practical durability evaluation. Consequently, the field of OER catalysis is entering a critical transition from pursuing high intrinsic activity to addressing long-term durability. Developing catalysts that remain stable under extreme industrial conditions has thus become a central challenge for both fundamental research and practical deployment.[33, 34]

Table 1. Key parameter differences between laboratory and industrial water electrolyzers.

Parameter	Laboratory	Industrial
Cell architecture	Three-electrode RDE	Flow cell, membrane electrode assembly (MEA), or zero-gap electrolyzer
Current density	10-100 mA cm^{-2}	>500 mA cm^{-2}
Temperature	Room temperature (20-25 °C)	Elevated temperature (70-80 °C)
Electrolyte	0.1 or 1.0 M KOH	20~40 wt% KOH
Operation time	Several to hundreds of hours	Thousands to tens of thousands of hours
Testing protocol	Constant current or potential	Dynamic load fluctuations, frequent start-stop cycling
Mass-transfer resistance	Small	Large
Cost and scalability	Small-scale research validation	Scalable practical application

In this review, we focus on the degradation mechanisms of OER performance under practical operating conditions using a multi-scale "micro-meso-macro" failure chain framework and discuss strategies to enhance durability. We first elucidate the sequential evolution of degradation, from atomic and molecular active-site reconstruction, to mesoscale structural instability, and ultimately to macro-scale performance decay at the electrolyzer, thereby establishing an integrated framework for understanding OER electrocatalysts deactivation. On this basis, we summarize key approaches for improving electrocatalyst stability. Operational stability can be effectively enhanced through integrated strategies involving intrinsic stability design, dynamic stability regulation, and rational optimization of operational conditions. These strategies encompass structural and electronic modulation and interfacial synergistic stabilization, catalyst activation and surface reconstruction, as well as regulation of the interfacial microenvironment, applied potential, and device components, collectively enabling long-term stable electrocatalytic operation. Finally, we summarize the current state of OER stability research and identify promising directions for future development. This review aims to stimulate deeper attention to OER degradation phenomena and provide valuable insights for the rational design of long-lived catalysts and devices for industrial water electrolysis.

2. The Multiscale Deactivation Mechanism of OER

The deactivation of OER electrocatalysts under practical operating conditions arises from a complex interplay of multiple factors, processes, and length scales. A systematic understanding of this phenomenon requires elucidating the intrinsic connections linking atomic- and molecular-scale evolution of active sites, nanoscale and microscale structural changes in catalyst particles and electrodes, and macroscopic performance decay at the device. Such a multiscale perspective provides critical insight into the deactivation mechanisms of OER electrocatalysts.

2.1 Microscale: Chemical Deactivation of Active Sites at the Atomic/Molecular Level

Microscale deactivation arises from atomic or molecular level changes in catalytic active sites and underlies OER performance degradation. Under high potentials and current densities, repeated oxidation-reduction cycles drive active centers away from thermodynamic stability. Dynamic active-site structures gradually destabilize, disrupting kinetically favorable configurations. Meanwhile, selective dissolution of

highly oxidized metal species induces surface stoichiometric imbalance, and lattice oxygen participation weakens the metal-oxygen framework. The accumulation of these processes ultimately limits long-term OER durability.

2.1.1 Dynamic Imbalance of Active-Site Evolution

In catalytic reactions, active-site structures are not fixed species; rather, they are dynamic, evolving units that can self-regulate and reconstruct in response to changing reaction conditions and electrochemical environments.[35, 36] The stability of a catalyst relies on the continuous generation and regeneration of these active-site structures. In electrocatalysis, maintaining the dynamic balance of active sites requires the presence of an intermediate reservoir, which supports the formation of reactive intermediates and ensures the ongoing regeneration of active-site structures. However, as the reaction progresses, if key species in the intermediate reservoir are irreversibly consumed, converted to inert species, or lost due to dissolution, the regeneration of active sites will be hindered, ultimately leading to catalyst deactivation.[37] This disruption is typically driven by the coupled effects of various factors, including applied potential, current density, and mass transport limitations, all of which together push the active-site structures towards irreversible evolution.[38]

Studies on the active-site evolution and kinetics of electrochemically driven CoO_xH_y transformations during the OER have revealed several complex structural evolution pathways. As shown in Fig. 1a, operando Raman spectroscopy captures an irreversible transformation from α-$Co(OH)_2$ to amorphous $CoO_x(OH)_{2-x}$ during the initial electrochemical cycle, followed by a reversible transition between amorphous $CoO_x(OH)_{2-x}$ and high-valent cobalt species $CoOOH_y$ at higher potentials.[39] Using atomically resolved identical-location TEM (IL-TEM), Dai et al. demonstrated that ZIF-67 undergoes dynamic phase evolution involving $Co(OH)_2$, active CoOOH, and inactive CoO during the OER (Fig. 1b). However, prolonged cycling gradually disrupts this evolving phase balance, and part of the $Co(OH)_2$ is consumed through irreversible chemical pathways. Consistently, TEM images of ZIF-67 after 300 cycles show severe skeletal collapse, with CoO nanoparticles and an amorphous surface layer indicative of a buildup of the inactive CoO phase (Fig. 1c).[40] Under acidic conditions, the Pourbaix diagram of RuO_2 (Fig. 1d) indicates that it is thermodynamically unstable under OER operation. The OER process induces the oxidation of stable Ru^{4+} to higher-valence $Ru^{n>4+}$ species, which accelerates dissolution and deactivation.[41] Similarly, Mn and Fe form soluble MnO_4^- and FeO_4^{2-} species at high potentials, leading to structural

View Article Online
DOI: 10.1039/D6SC03869G

instability (Fig. 1e), consistent with experimentally observed high-potential degradation of Mn-based catalysts.[14] Therefore, catalyst design should prioritize the stability and regeneration of dynamic active sites, minimizing active-site loss while preserving the intermediate reservoir to extend catalyst lifetime.

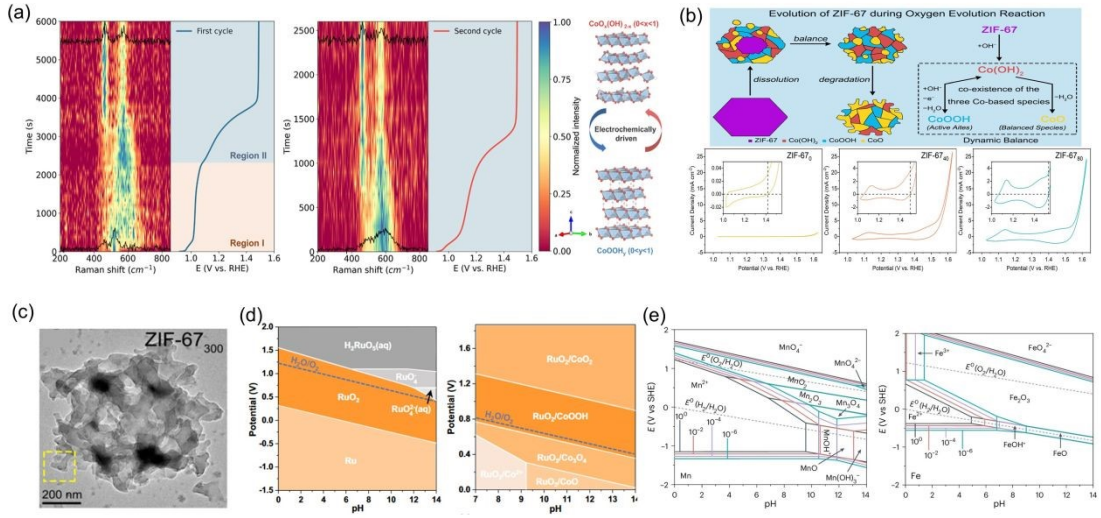

Fig. 1 (a) Operando Raman spectra of the CoO_xH_y thin film under CP measurement at a constant current of 10 μA. A "reset" process (holding at 0.885 V vs RHE over 6 min) was conducted between these two cycle tests. Reproduced with permission.[39] Copyright 2022, American Chemical Society. (b) Evolution of ZIF-67 during OER and cyclic voltammetry (CV) curves at various cycling stages. (c)TEM images of ZIF-67_{300}. Reproduced with permission.[40] Copyright 2025, American Chemical Society. (d) Calculated Pourbaix diagrams of RuO_2 and RuO_2/CoO_x, respectively. Ion concentrations are 10^{-6} M. Reproduced with permission.[41] Copyright 2022, Springer Nature. (e) Pourbaix diagrams of manganese and iron, highlighting the potential-pH stability regions across ion concentrations from 1×10^{-6} to 1×10^{0} mol L^{-1}. Reproduced with permission.[14] Copyright 2024, Springer Nature.

2.1.2 Selective Dissolution and Surface Stoichiometric Imbalance

For catalysts composed of multiple metals, the deactivation pathways are often closely associated with the selective dissolution of metal cations. The leaching behavior of these cations is highly complex under operating conditions and is influenced by factors such as the local coordination environment and the applied potential. A key mechanistic feature is that the metal centers undergo oxidation-state elevation, coordination perturbation, and M-O bond weakening under anodic polarization, thereby exhibiting crystallographic orientation dependence and defect-selective dissolution behavior.[42-44] To quantitatively evaluate catalyst stability, the stabilization number (S-number), defined as the number of O_2 molecules produced per dissolved metal atom, is particularly useful for assessing dissolution-related degradation. To evaluate other deactivation pathways, such as phase/morphology reconstruction, interfacial passivation, bubble-induced detachment, or device-level degradation, additional or

alternative evaluation metrics should be established. Conventional electrochemical techniques, including cyclic voltammetry (CV), chronoamperometry (CA), and chronopotentiometry (CP), are also commonly employed for stability evaluation. Among them, CV evaluates catalyst stability under transient conditions over a wide potential window, whereas CA and CP reflect stability under steady-state conditions at constant potential and current density. Although these methods have been widely used, sometimes the stability information obtained by these methods is inconsistent. In particular, the cathodic polarization occurring during CV scanning can partially counteract the structural and chemical degradation induced by anodic polarization. In contrast, CA evaluates stability under constant electro-oxidation conditions, whereas the continuously varying potential during CP measurements results in dynamically changing oxidation environments. Therefore, multiple electrochemical methods should be combined to comprehensively evaluate catalyst stability.[16]

Taking NiFe-LDH as an example, Peng et al. found that LDH structures are not stable under alkaline OER conditions. Although the incorporation of Fe significantly enhances the intrinsic activity of Ni-based catalysts, Fe is highly susceptible to dissolution. The concentrations of dissolved metal ions in the electrolyte after CV and CA measurements were quantified by ICP-OES. As shown in Fig. 2a, after CV scanning, the concentrations of Ni and Fe ions dissolved in the electrolyte are comparable for all four catalysts, indicating that the observed activity loss cannot be attributed to a reduction in the number of active sites caused by metal dissolution during OER. In contrast, following CA testing, pronounced differences in the concentrations of Ni and Fe ions are observed in the electrolyte, which correlate strongly with the extent of OER activity decay (Fig. 2b). These results suggest that during sustained OER operation, Fe^{3+} leaches out from the layered structure into the electrolyte, thereby disrupting the original surface stoichiometry of the catalyst (Fig. 2c). This dissolution is not spatially uniform; instead, it preferentially occurs at high-energy sites or structural defects. As illustrated in Fig. 2d, theoretical calculations further confirm that this process generates vacancies and alters the local structure. In addition, the dissolved ions may redeposit at other locations on the catalyst surface, forming NiOOH and FeOOH phases. Such dynamic redistribution can induce reconstruction or aggregation of originally isolated active sites.[45]

View Article Online
DOI: 10.1039/D6SC03869G

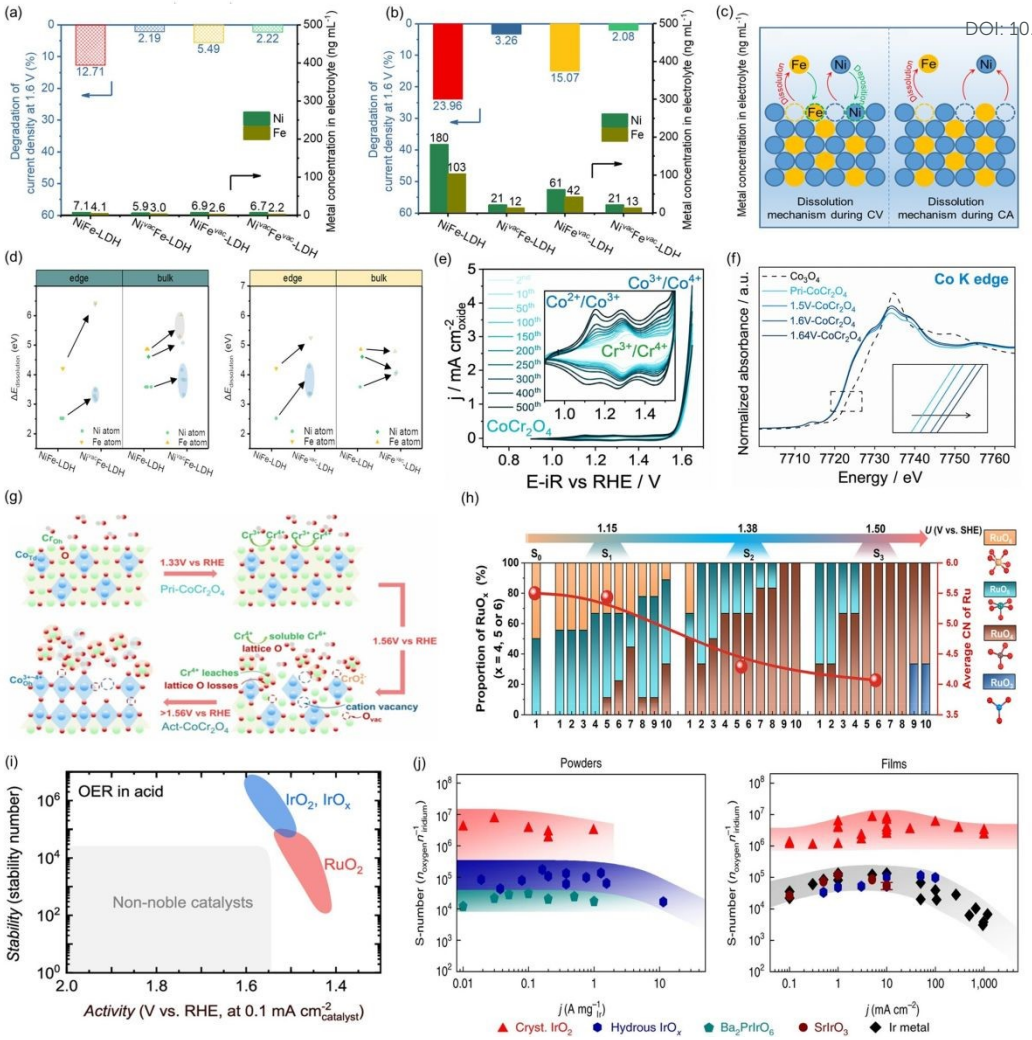

Fig. 2 Summary of activity loss and metal dissolution in NiFe-LDH during CV (a) and CA (b) processes. (c) Schematic illustration of the metal dissolution mechanism. (d) DFT (Density Functional Theory) calculated dissolution energies of metal atoms in NiFe-LDH with M^{2+} and M^{3+} vacancies. Reproduced with permission.[45] Copyright 2021, Wiley. (e) CV cycling behavior and (f)Co K-edge XANES evolution of $CoCr_2O_4$ in 1 M KOH under different applied potentials. (g) Scheme of $CoCr_2O_4$ surface change before OER testing after being applied increased potentials. Reproduced with permission.[46] Copyright 2021, Wiley. (h) Percentage histogram for the proportion of different RuO_x units (x = 3, 4, 5, and 6). Reproduced with permission.[47] Copyright 2025, American Chemical Society. (i) Potential-driven structural evolution and stabilization mechanism of RuO_2 and activity-stability map in acidic OER. Reproduced with permission.[48] Copyright 2023, American Chemical Society. (j) S-number plotted versus mass-specific current density for powders and geometric current density for sputtered films. Reproduced with permission.[49] Copyright 2018, Springer Nature.

For spinel, the selective dissolution of different metal species likewise governs surface reconstruction and the evolution of catalytic activity. Xu et al. revealed the controlled leaching behavior of Cr in $CoCr_2O_4$. As shown in Fig. 2e, during CV measurements, increasing the applied potential from 1.5 to 1.7 V gradually suppresses the Cr^{4+}/Cr^{3+} redox couple, while redox transitions associated with Co^{2+}/Co^{3+} and Co^{3+}/Co^{4+} become dominant. This behavior indicates that only after activation at

View Article Online
DOI: 10.1039/D6SC03869G

sufficiently high anodic potentials does $CoCr_2O_4$ expose Co-rich electrochemically active centers to the alkaline electrolyte. XANES analysis indicates the formation of Co oxyhydroxide species at potentials above 1.6 V, while the average Co oxidation state remains almost unchanged after holding at 1.5 V for 7 h. ^{18}O isotope labeling further confirms that lattice oxygen does not participate in the OER but instead dissolves into the electrolyte, likely due to the generation of Cr^{6+} (Fig. 2f,g).[46] However, whether the resulting CoOOH arises from the direct oxidation of tetrahedrally coordinated Co^{2+} or from a dissolution-redeposition pathway remains under debate, and direct evidence of the structural evolution is still required from advanced operando techniques such as extended X-ray absorption fine structure (EXAFS) and environmental transmission electron microscopy (ETEM).

Similar dissolution behavior induced by high-valent metal states is also observed in noble metal oxides. Taking RuO_2 as an example, Li et al. employed an adaptive machine-learning framework to statistically analyze the potential-dependent population of surface RuO_x coordination units (RuO_6, RuO_5, and RuO_4) on RuO_2(110), thereby directly elucidating the selective dissolution and structural evolution of Ru active sites during acidic OER. Their results show that, at relatively low potentials, the self-evolved distorted RuO_5 units constitute a metastable active state, which is characterized by only minor Ru dissolution accompanied by a moderate activity self-enhancement (Fig. 2h). However, this state possesses a low potential resistance capability (PRC) and evolves into inert RuO_4 units at elevated potential. This transformation is accompanied by significant rearrangement of the oxygen coordination environment and continuous weakening of Ru-O bonds, ultimately triggering rapid Ru dissolution.[47] In contrast, IrO_2 exhibits substantially higher structural stability during acidic OER, with its active components being far less prone to excessive oxidation or dissolution compared to Ru-based oxides (Fig. 2i).[48] When quantified using the S-number as a stability metric, the durability of different catalysts can differ by several orders of magnitude, with Ir-based catalysts typically displaying much higher S-numbers, thereby highlighting their superior resistance to degradation in acidic environments (Fig. 2j).[49]

Selective catalyst dissolution underpins performance degradation, and the development of robust stability metrics and electrochemical operando characterizations enables quantitative stability assessment across different catalyst systems.

2.1.3 Lattice Oxygen Evolution

The lattice oxygen mechanism (LOM) has emerged as an effective strategy to enhance the intrinsic activity of metal oxide catalysts for OER, as it circumvents the linear scaling relationships between intermediate adsorption energies inherent to the conventional adsorbate evolution mechanism (AEM) (Fig. 3a).[50] The key to triggering LOM is that the nonbonding oxygen 2p state must be located above the lower Hubbard band (LHB) and close to the Fermi level (Fig. 3b).[51] However, under anodic polarization, the position of the O 2p band is strongly coupled to the surface stability and reconstruction behavior of oxide catalysts. For example, Liu et al. compared a series of metal oxides and found that when the O 2p band center is approximately -2.7 eV, lattice oxygen participation reaches its optimal level, resulting in the highest OER activity, as shown in Fig. 3c. In contrast, excessive upward shifting of the O 2p level over activates lattice oxygen, disrupts energy alignment, and destabilizes the structure, ultimately diminishing catalytic activity and stability.[52] Further research by Shao-Horn et al. revealed that when the O 2p level is close to the Fermi level, $La_{0.5}Sr_{0.5}Co_{0.8}Fe_{0.2}O_{3-\delta}$ undergoes rapid surface reconstruction during OER. In contrast, for oxides such as $La_{0.4}Sr_{0.6}CoO_{3-\delta}$ and $LaCoO_{3-\delta}$, where the oxygen 2p levels are far from the Fermi level, the surface retains its crystalline integrity after the reaction.[53] Moreover, many studies have pointed out that the position of the O 2p band is closely related to the oxygen vacancy formation energy: as the O 2p band approaches the Fermi level, the oxygen vacancy formation energy decreases, increasing oxygen ion diffusion.[54]

View Article Online
DOI: 10.1039/D6SC03869G

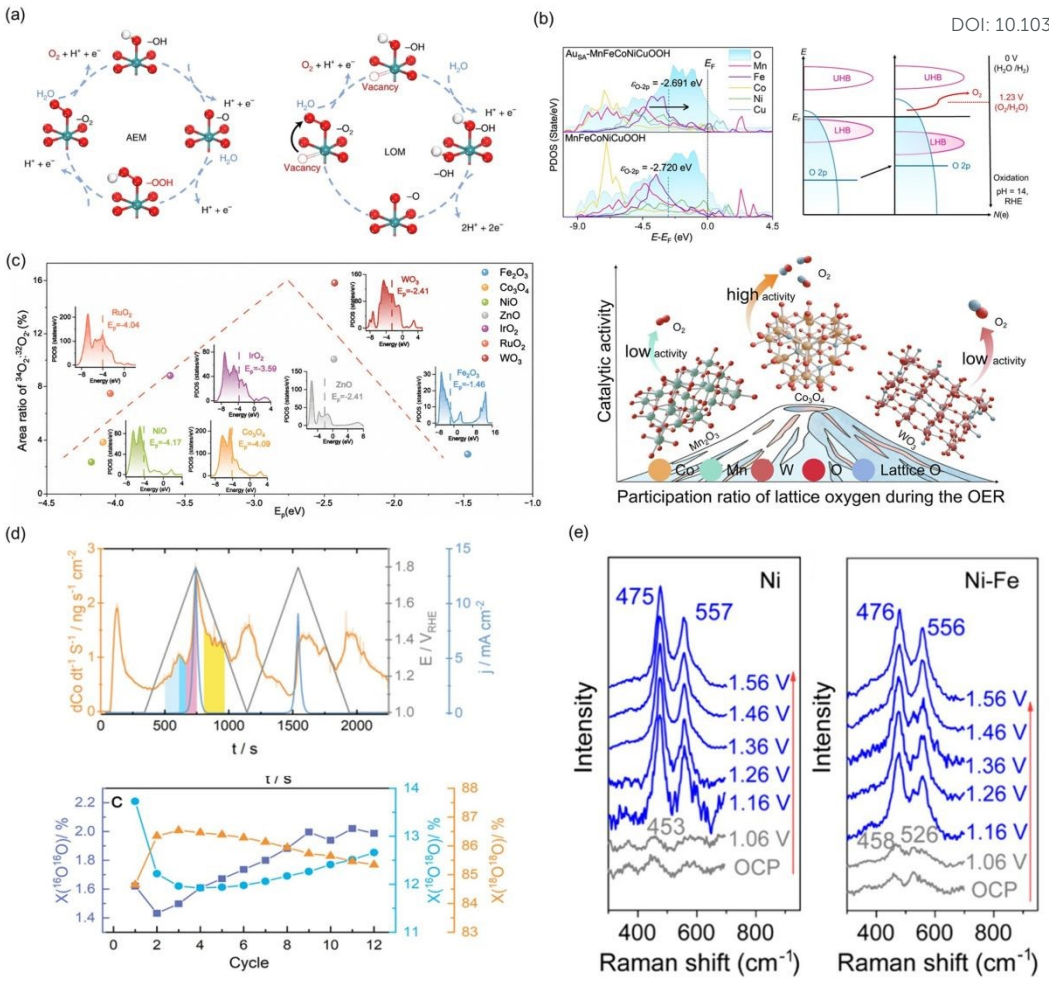

Fig. 3 (a) Schematic illustration of simplified OER mechanisms for AEM and LOM. Reproduced with permission.[50] Copyright 2021, Springer Nature. (b) Projected density of states (E_F: Fermi level, ε_{O-2p}: O 2p band center) and schematic band diagrams (UHB: upper Hubbard band, LHB: lower Hubbard band, N(e): state density. Reproduced with permission.[51] Copyright 2023, Springer Nature. (c) Trend of the $^{34}O_2/^{32}O_2$ ratio for seven metal oxide catalysts in LOM vs. O 2p band center, and schematic volcano plot of lattice oxygen participation and OER activity. Reproduced with permission.[52] Copyright 2025, Elsevier. (d) Dissolution profiles of cobalt in Co_3O_4 during the CV measurements with the LPL of 1.00 V_{RHE} and DEMS results for the start-up/shutdown protocol recorded with OM-Co_3O_4. Reproduced with permission.[55] Copyright 2025, American Chemical Society. (e) In situ Raman spectra of the Ni and Ni-Fe. Reproduced with permission.[56] Copyright 2024, American Chemical Society.

From a mechanistic perspective, the involvement of lattice oxygen implies that oxygen vacancies are generated during each OER cycle. Although a moderate amount of oxygen vacancies can tune the electronic structure and enhance catalytic activity, the dynamic replenishment of these vacancies is crucial during the LOM process. Insufficient replenishment leads to continuous vacancy accumulation, which ultimately induces lattice distortion and even structural collapse. This is particularly evident in spinel structures containing redox-active metals (e.g., Co^{2+}/Co^{3+}), where excess oxygen vacancies can disrupt the spinel framework, causing the catalyst to transition from a

crystalline to an amorphous state, and even eventually dissolve.[57] Priamushko et al. used spinel Co_3O_4 as a model catalyst to reveal transient Co dissolution under acidic OER conditions. Pronounced dissolution peaks appear during both anodic oxidation and cathodic reduction, correlating with the formation of high-valence Co species at high potentials. Differential electrochemical mass spectrometry (DEMS) measurements further verify lattice oxygen evolution during the OER, indicating that lattice oxygen participation is intrinsically coupled with transient metal dissolution and structural evolution (Fig. 3d).[55] Jing et al. observed that the Raman spectra of O^{18}-labeled γ-NiOOH shifted by 15 and 17 cm^{-1} compared to O^{16}-NiOOH. After continued OER reactions in $KO^{16}H$ solution, the Raman peaks shifted back to 475 and 557 cm^{-1}, demonstrating the lattice oxygen oxidation mechanism of γ-NiOOH, with a significantly increased risk of structural instability (Fig. 3e).[56] Thus, while utilizing the LOM mechanism to enhance activity, how to effectively stabilize lattice oxygen or promote rapid healing of oxygen vacancies remains one of the key challenges in the design of high-performance OER electrocatalysts.

2.2 Mesoscale: Structural Instability at the Nano/Microscale

As the scale of deactivation extends from the atomic/molecular level to the nano- and micron-scale, involving millions of atoms, the deactivation mechanism becomes more complex, manifested by the degradation of overall structural integrity and the dynamic evolution of catalyst morphology. These processes are often determined by thermodynamic and kinetic factors and are closely related to the synthesis method and microstructure. The evolution is triggered by dissolution-reprecipitation, valence state migration, and local reconstruction at the microscopic scale, while amplified by current distribution, bubble evolution, ultimately leading to structural instability of the catalyst.

2.2.1 Surface Reconstruction

The structural evolution commonly undergone by electrocatalysts during operation is collectively referred to as reconstruction. With the rapid advancement of in situ and operando characterization techniques, the dynamic evolution of catalyst surfaces and near-surface regions can now be directly monitored under realistic electrochemical conditions. Electrochemical dynamic reconstruction typically transforms pre-catalysts into amorphous or low-crystallinity active phases with high activity, thereby lowering the energy barrier for the OER. Reconstruction can be understood from three interrelated aspects: triggering conditions, reconstruction rate,

View Article Online
DOI: 10.1039/D6SC03869G

and reconstruction degree. The triggering conditions define the onset potential and environmental parameters, including temperature, electrolyte concentration, and overpotential.[58, 59] The reconstruction rate reflects the kinetic ease of structural transformation, where faster reconstruction accelerates the generation of active sites and enhances overall water electrolysis efficiency. The reconstruction degree describes the fraction of catalyst converted into active species, with higher degrees leading to deeper reconstructed layers, greater active-site exposure, and improved catalyst utilization.

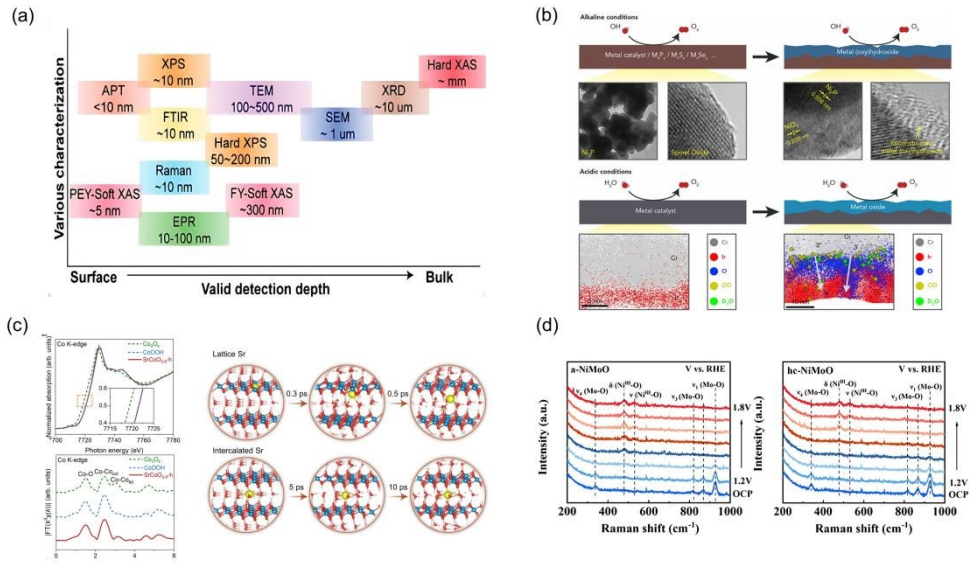

Fig. 4 (a) Schematic illustration for various characterizations with valid detection depth. Reproduced with permission.[60] Copyright 2023, Wiley. (b) Surface reconstruction of electrocatalysts during OER under alkaline and acidic conditions. In alkaline media, transition metals and their compounds reconstruct into metal (oxy)hydroxides, whereas under acidic conditions, metal-based catalysts transform into metal oxides. Reproduced with permission.[61] Copyright 2021, Elsevier. (c) Co K-edge XANES spectra and K-edge FT-EXAFS spectra and AIMD simulations of Sr in γ-CoOOH. Reproduced with permission.[62] Copyright 2025, American Chemical Society. (d) Operando Raman spectra of a-NiMoO and hc-NiMoO. Reproduced with permission.[63] Copyright 2025, Wiley.

Numerous in situ and operando studies, including X-ray absorption spectroscopy (XAS), Raman spectroscopy, and electrochemical mass spectrometry (Fig. 4a), [60] consistently demonstrate that most 3d transition-metal oxides/hydroxides undergo pronounced surface self-reconstruction under alkaline OER conditions (Fig. 4b),[61] forming metal oxide/hydroxide dominated active phases. For example, Xue et al. combined XAS and ab initio molecular dynamics simulations (AIMD) to demonstrate that during the electrochemical reconstruction of $SrCoO_{3-\delta}$, A-site Sr^{2+} ions are not fully dissolved but partially intercalate into the interlayers of newly formed γ-CoOOH,

thereby critically regulating active-phase formation and catalytic performance (Fig. 4c).[62] He et al. further proposed a dual-regulation strategy involving structural disorder and oxidizable Mo^{6+}, enabling controlled reconstruction of Ni-based pre-catalysts into highly disordered NiOOH. Structural disorder lowers the reconstruction onset potential, while Mo^{6+} dissolution induces metal-site vacancies and enhances Ni-O covalency, driving a transition from AEM to LOM and markedly improving activity (Fig. 4d).[63] Such processes are characteristic of beneficial reconstruction (Fig. 5a), in which amorphous phases with high defect densities and abundant exposed active sites reduce overpotentials and accelerate intrinsic kinetics.[64, 65] In contrast, reconstruction can also be detrimental (Fig. 5b).[66] In some systems, performance degradation can result from the leaching of active elements, the formation of inert phases, or the poisoning of active species. Deka et al. showed that as the potential increases, the oxidation state of Ru continuously rises, leading to the over-oxidation of lattice oxygen and subsequent lattice collapse. This process forms thermodynamically stable, higher-valent inert RuO_x species and soluble Ru species, accompanied by severe activity loss.[67]

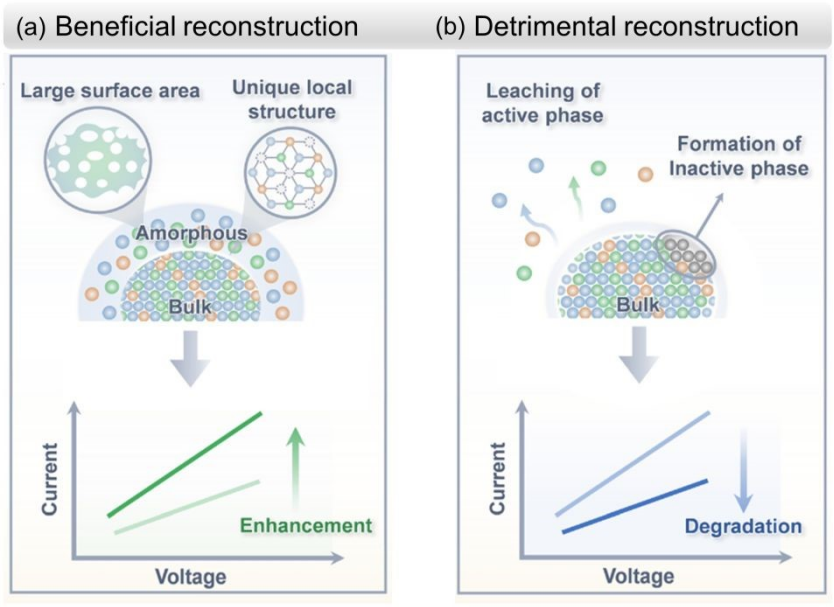

Fig. 5 Schematic of beneficial (a) and detrimental (b) reconstruction. Reproduced with permission.[66] Copyright 2025, Royal Society of Chemistry.

Surface reconstruction represents an adaptive response of electrocatalysts to the electrochemical interfacial microenvironment (Fig. 6). The primary driving factors can be summarized as follows: (1) Higher applied potentials not only overcome reaction energy barriers and accelerate surface reconstruction, but also regulate the adsorption, desorption, and transformation kinetics of reactants at the electrode-electrolyte

interface, thereby dictating the structural evolution pathways.[68] (2) Strongly adsorbed intermediates (*O and *OH) which modify local electronic structures and bonding strengths and can induce atomic rearrangements.[69] (3) The interfacial electrolyte species such as CO_2, OH^-, and halide ions, as well as electrolyte concentration and pH, which collectively govern adaptive surface evolution and influence reaction selectivity and kinetics.[70, 71]

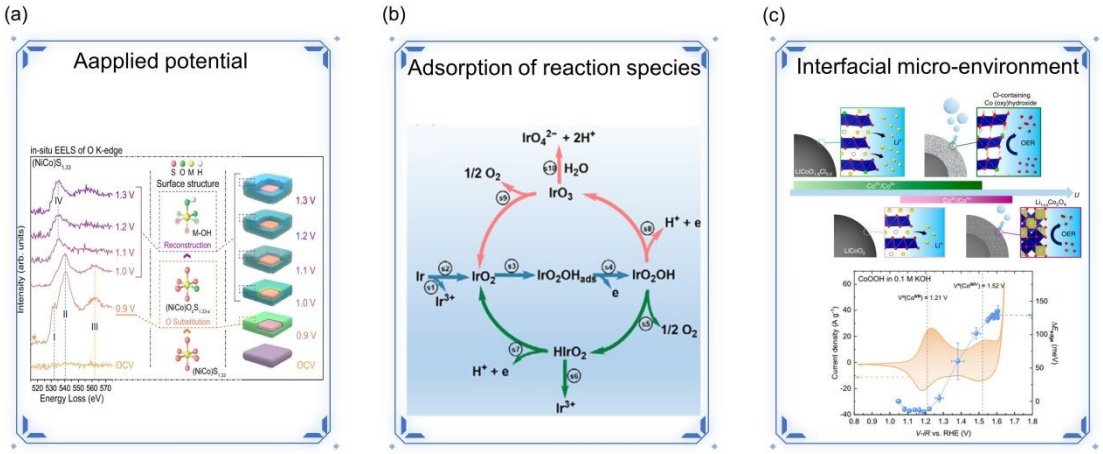

Fig. 6 Factors influencing catalyst surface reconstruction. (a) Reproduced with permission.[68] Copyright 2023, Springer Nature. (b) Reproduced with permission.[69] Copyright 2022, Elsevier. (c) Reproduced with permission.[70, 71] Copyright 2021 and 2025, Springer Nature.

Overall, beneficial reconstruction can construct robust active configurations conducive to long-term operation, while detrimental transformation may lead to rapid deactivation. This delicate balance between activity enhancement and structural degradation highlights the critical importance of understanding and controlling reconstruction processes in electrocatalyst design, with specific modulation strategies discussed in the following sections.

2.2.2 Insufficient Mechanical Strength of Nanostructures

At the nano- and microscale, geometric morphology affects not only the distribution of three-phase interfaces and local current density but also mechanical stress concentration and bubble behavior. Regions with high curvature and high surface energy, such as the tips and edges of nanorod, nanowire, or nanoneedle arrays, exhibit pronounced electric-field and current-density localization,[72] making them both highly active reaction sites and preferential initiation points for pitting and structural fracture. Using CoNi oxyhydroxide nanostructures with varying aspect ratios as OER model electrodes, Ran et al. demonstrated that nanorods with high aspect ratios underwent

significant structural disintegration during durability testing, while their nanoplate counterparts with identical composition remained intact, exhibiting superior stability (Fig. 7a). Finite element analysis (Fig. 7b) further revealed that the small radii of curvature at tips and edges markedly amplify local current density and reaction rates, demonstrating that aspect ratio and curvature alone can dictate mechanical lifetime, even with identical composition and surface states.[73]

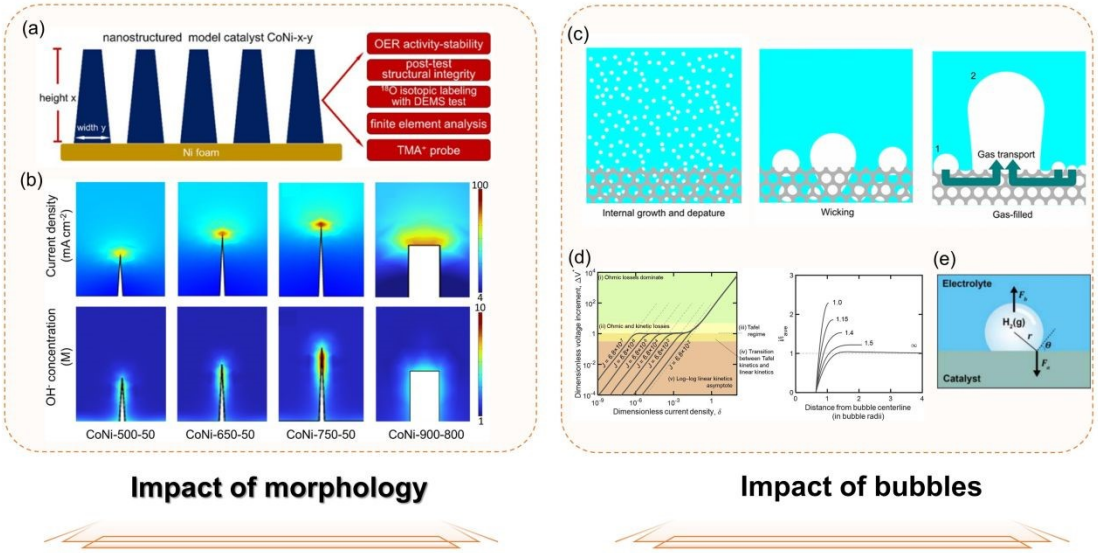

Fig. 7 (a)The schematic illustration of model catalysts with different nanostructures. (b) Local current density distribution and local OH^- ion concentration distribution among various model catalysts. Reproduced with permission.[73] Copyright 2025, Royal Society of Chemistry. (c) Schematics of the internal growth and departure mode, the wicking mode, and the gas-filled mode. Reproduced with permission.[74] Copyright 2025, Elsevier. (d) Effect of Attached Bubbles in the Potential Increment and Electrode-Current Distribution. Reproduced with permission.[75] Copyright 2020, Elsevier. (e) Schematic illustration of force analysis acting on the bubble adhered to the catalyst surface. Reproduced with permission.[76] Copyright 2023, Wiley.

Beyond morphology, bubble generation and evolution during OER constitute another critical factor driving structural instability. Bubbles trapped within cracks or pores exacerbate mechanical damage through volumetric expansion, while bubbles covering the catalyst layer block active sites, reduce the effective reaction area, and force current to concentrate through the remaining exposed regions, thereby amplifying local stress and accelerating deactivation.[14] In gas-evolving electrodes, bubble dynamics generally manifest in three characteristic modes (Fig. 7c): internal growth and detachment, capillary wicking and gas-filling, arising from distinct mechanisms of bubble nucleation, growth, and release.[74] Adhered bubbles markedly reduce the electrochemically active surface area, leading to increased activation overpotentials at a fixed current density. The current density is therefore closely coupled to bubble

coverage: at low current densities, kinetic losses dominate, whereas at very high bubble coverage, the activation overpotential is governed almost entirely by bubble blocking; at high current densities, ohmic losses become the primary contribution. Moreover, the dynamic evolution of bubbles induces persistent current inhomogeneity across the electrode surface (Fig. 7d),[75] and the transient tensile forces generated during bubble detachment impose additional mechanical loading on the catalyst layer, ultimately causing mechanical damage and catalyst failure (Fig. 7e).[76]

Consequently, understanding and regulating the synergistic interplay between geometric morphology and bubble dynamics is essential for designing practical water electrolysis electrodes that combine high activity with robust stability.

2.2.3 Catalyst Layer Delamination Driven by Ripening and Agglomeration

The evolution of particle size can markedly alter catalyst surface morphology, leading to a decrease in electrochemically active surface area (ECSA) and an increase in reaction overpotential, ultimately resulting in severe catalyst deactivation or even dissolution. Among the underlying causes, Ostwald ripening and particle agglomeration represent two of the most common and strongly interconnected driving mechanisms. During Ostwald ripening, smaller particles preferentially dissolve, and the dissolved species subsequently redeposit onto thermodynamically more stable larger particles, giving rise to a continuous increase in the average particle size. Xu et al. directly observed pronounced ripening behavior during the electrocatalytic operation of Ge-RuO_2, ultimately leading to the formation of valence-separated aggregates (a-Ge-RuO_2) as shown in Fig. 8a. Further HAADF-STEM characterization in Fig. 8b revealed that both large crystallites and residual small particles evolve toward low-index crystal facets.[77] Besides ripening, high surface energy drives nanoparticle agglomeration, a process often accompanied by substantial lattice strain relaxation and volumetric contraction. As neighboring particles coalesce, the resulting aggregates tend to densify. Sharma et al. investigated agglomeration in the deactivation of Ag nanoparticles using TEM in Fig. 8c, finding that Ag clusters block active sites and reduce electrode wettability.[78] Similarly, Bizzotto et al. reported that at high Ir loadings (70 wt%), IrO_2 nanoparticles undergo localized agglomeration on carbon supports, causing a pronounced decrease in ECSA and a concomitant loss in OER mass activity (Fig. 8d,e).[79]

View Article Online
DOI: 10.1039/D6SC03869G

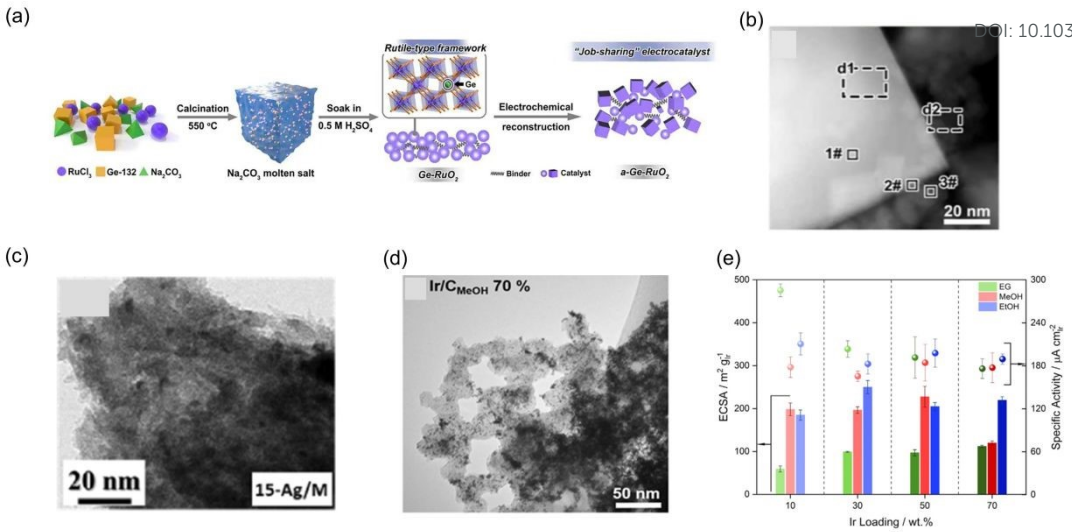

Fig. 8 (a) Schematic illustration of the synthetic route for a-Ge-RuO_2. (b) HAADF-STEM images of a-Ge-RuO_2. The inset shows the magnified image of the bulk (d1) and particle (d2). Reproduced with permission.[77] Copyright 2025, Wiley. (c) TEM images depicting the agglomeration of AgNPs. Reproduced with permission.[78] Copyright 2023, Elsevier. (d) TEM image of Ir/C (70 wt%) prepared using MeOH. (e) ECSA (CO stripping) and specific activity of Ir-based catalysts as a function of metal loading. Reproduced with permission.[79] Copyright 2021, Elsevier.

Notably, ripening and agglomeration mutually reinforce each other. Within agglomerates, restricted mass transport facilitates local supersaturation, which in turn accelerates ripening. Ultimately, these large particles or dense aggregates may detach from the electrode surface due to weakened physical adhesion or mechanical perturbations, leading to catalyst layer delamination. To mitigate such degradation pathways, strategies commonly involve introducing strong metal-support interactions to anchor metal nanoparticles or employing elemental doping to lower surface energy, thereby enhancing the thermodynamic stability of the nanostructured catalysts.

2.3 Macroscopic Scale: Degradation Driven by Operating Conditions

Even when electrocatalysts are optimally engineered at the atomic and mesoscale levels, their performance and lifetime in practical electrolyzers remain strongly influenced by complex operating conditions. These system-level effects often act as the decisive factors that ultimately trigger catalyst failure.

Start-Stop Cycling. Under practical operating conditions, electrolyzers inevitably undergo frequent start-stop cycling, during which catalysts are repeatedly exposed to transitions between the OER operating potential and the open-circuit potential. Such start-stop cycling triggers a distinct degradation pathway, commonly referred to as low-potential corrosion, which is rarely observed under constant potential operation.[80, 81] Alia et al. systematically investigated the performance decay induced by redox

View Article Online
DOI: 10.1039/D6SC03869G

transitions of catalysts during simulated start-stop operation and developed an accelerated stress test protocol. This protocol employs low catalyst loadings, frequent start-stop cycling, and elevated peak potentials to accelerate degradation and thereby reduce experimental time. Compared with intermittent or load-cycling accelerated tests, frequent redox-driven start-stop cycling increases the degradation rate from 3.2 to 5.5 $\mu V \cdot cycle^{-1}$ (Fig. 9a). The performance loss is primarily attributed to the reduction of subsurface iridium and its subsequent rapid dissolution at high potentials.[82]

Component-Induced Instability and Lifetime Reductions. The degradation of OER electrocatalysts is not confined to anodic activity loss; it can propagate through species transport and interfacial evolution to inflict collateral damage on other critical stack components, thereby accelerating overall lifetime decay. For instance, detached catalyst particulates may lodge within membrane/separator pathways, increasing ion transport resistance and even leading to local short circuits. In PEMWEs, the high anodic potential may enable H_2O_2 generation followed by radical formation, which in turn drives membrane chemical degradation and structural deterioration (Fig. 9b).[83] Moreover, interface degradation between the catalyst layer and the PTL interface can impair interfacial contact and increase the interfacial resistance, amplifying ohmic losses and further accelerating performance decay (Fig. 9c).[84] Corrosion of bipolar plates under acidic or alkaline conditions may also be exacerbated during catalyst failure. Collectively, these cross-component, mutually reinforcing failure pathways render OER electrocatalysts stability a system-level challenge that couples materials, interfaces, electrochemistry, and transport processes.

Harsh Working Environment. Electrocatalytic performance is typically evaluated under comparatively mild laboratory conditions, whereas practical operation in industrial electrolyzers is substantially harsher, as discussed in Table 1. Consequently, electrocatalysts that appear highly active under benign conditions do not necessarily deliver equivalent catalytic capability in industrial cells. However, catalysts that perform well under mild conditions do not always translate to industrial electrolyzers, where high temperature, concentrated electrolytes, high pressure, and fast flow reshape kinetics and mass transport, accelerating nanostructure degradation.[85, 86] For example, increasing the temperature from 25.0 to 51.9 °C completely reconstructed a $NiMoO_4$ catalyst into stable (oxy)hydroxides (NiOOH) featuring abundant boundaries, which served as the real OER active sites and exhibited enhanced catalytic activity. This temperature-driven reconstruction was corroborated by in situ low-/high-temperature

View Article Online
DOI: 10.1039/D6SC03869G

Raman spectroscopy, together with ex situ microscopy and electron tomography (Fig. 9d).[87]

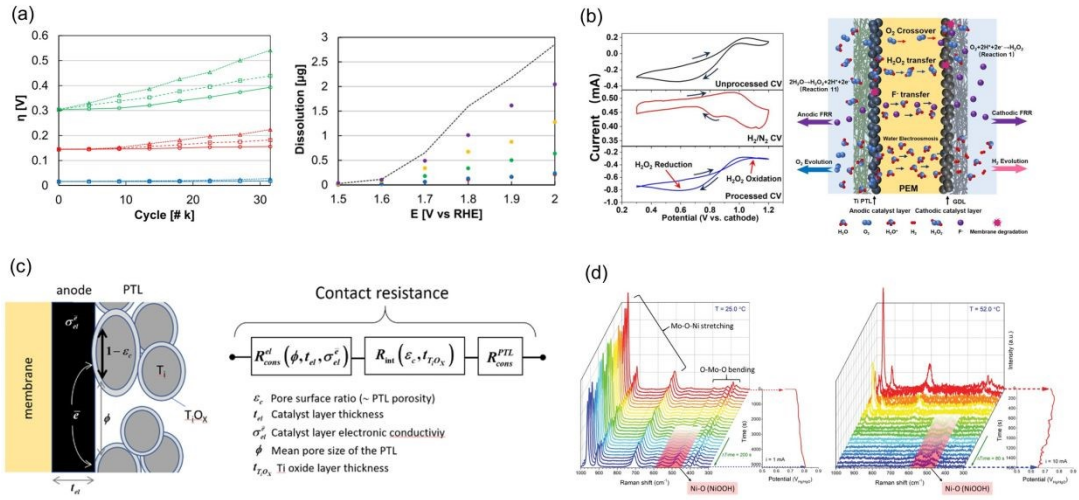

Fig. 9 (a) Overpotential changes at 1 A cm^{-2} and dissolution after 13.5 h potential cycling between an upper potential (x-axis) and a lower potential (1.4, 1.0, 0.6, 0.4, or 0 V). Reproduced with permission.[82] Copyright 2024, The Electrochemical Society. (b) Schematic illustration of membrane degradation in PEMWEs using Nafion 212 and Nafion/1% CeO_2 composite membranes. Reproduced with permission. Reproduced with permission.[83] Copyright 2024, Royal Society of Chemistry. (c) Electron transfer at the catalyst layer/PTL interface for PTLs with different pore sizes. Reproduced with permission.[84] Copyright 2024, Elsevier. (d) In situ high-temperature Raman spectra and corresponding chronopotentiometric curve of $NiMoO_4$ pre-catalyst in 1 m KOH at 52.0 °C. Reproduced with permission.[87] Copyright 2020, Wiley.

In practical electrolyzers, catalyst degradation is predominantly driven by operating-condition-induced rather than intrinsic instability of active sites. Frequent start-stop cycling imposes repeated redox potential excursions, accelerating dissolution-related degradation pathways. In addition, particle detachment and interfacial evolution can damage critical components and amplify performance decay. Meanwhile, harsh industrial conditions, including elevated temperature, pressure, and strong electrolyte convection, further accelerate structural degradation. Therefore, catalyst stability and system compatibility must be jointly optimized and rigorously evaluated under realistic operating conditions and dynamic loads to enable efficient and durable long-term electrolyzer operation.

Overall, catalyst degradation originates from the coupled effects of microscopic chemical instability, mesoscopic structural evolution, and macroscopic operational conditions, which collectively determine long-term catalytic stability. At the microscopic scale, active-site instability, selective metal dissolution, and lattice oxygen participation highlight the need to stabilize dynamic active structures under highly

oxidizing conditions, while improving the reversibility of active-site evolution, suppressing irreversible metal loss, and balancing lattice oxygen activity with structural stability. At the mesoscopic scale, degradation is associated with uncontrolled surface reconstruction, nanostructural fracture, particle agglomeration, and catalyst-layer delamination, emphasizing controllable reconstruction, robust nanostructures, and stable catalyst-support coupling. At the macroscopic scale, start-stop cycling, elevated temperatures, high current densities, and component degradation further accelerate failure. Therefore, future strategies should integrate catalyst adaptability with electrolyzer-level optimization. Specific stabilization strategies will be discussed in the subsequent sections.

3 Strategies for Enhancing Operational Stability

In practical applications, the stability of electrocatalysts often constitutes a critical bottleneck limiting their long-term and efficient operation. To address this challenge, a variety of operational stability enhancement strategies have been proposed in recent years, primarily focusing on intrinsic stability design, complemented by dynamic stability regulation and optimization of operating conditions, thereby enabling stable catalyst performance under high potentials and prolonged operating durations.

3.1 Designing Intrinsically Stable OER Electrocatalysts

The intrinsic stability of a catalyst, defined by the inherent resistance of its original crystal structure and chemical composition to corrosion and structural transformation under harsh electrochemical environments, dictates its ability to withstand dissolution, structural collapse, and loss of active sites at high potentials, thereby forming the foundation for long-term stable operation. Consequently, constructing robust chemical bonding and stable crystal frameworks through rational materials engineering represents a primary prerequisite for enhancing the stability of OER electrocatalysts.

3.1.1 Regulating Structure

Tuning the exposed crystal facets has emerged as an effective strategy to control surface reconstruction. Facet identity is intimately coupled with catalytic activity and durability, as well as with structural reconstruction under operating conditions. Distinct facets govern the adsorption of reactants, the distribution of active sites, and the preferred reaction pathways, thereby exerting decisive control over overall catalytic behavior.

View Article Online
DOI: 10.1039/D6SC03869G

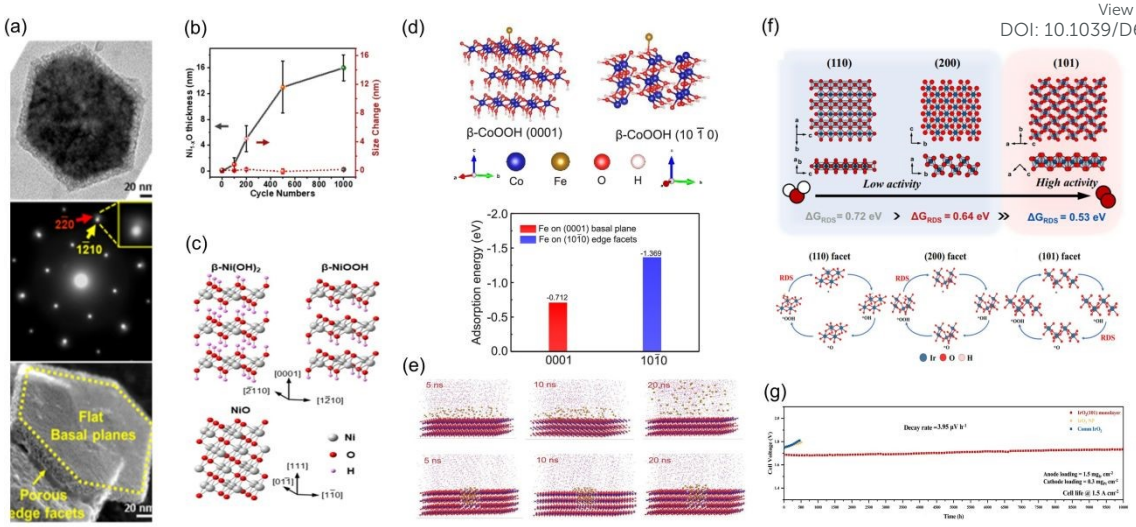

Fig. 10 (a) TEM, SAED, and BSE-STEM characterization of pristine β-$Ni(OH)_2$. (b) $Ni_{1-x}O$ layer thickness and platelet size change versus CV cycle number under the OER window (1.1-1.6 V). (c) Atomic structure of β-$Ni(OH)_2$, β-NiOOH, and NiO. Reproduced with permission.[88] Copyright 2024, American Chemical Society. (d) Fe adsorption on β-CoOOH basal and edge facets. (e) Fe^{3+} diffusion in aqueous alkaline solution at different times. Reproduced with permission.[89] Copyright 2023, American Chemical Society. (f) Rutile IrO_2 facet models and corresponding OER Gibbs free-energy diagrams at 1.23 V. (g) Steady-state durability of an IrO_2(101) monolayer, delivering >10,000 h OER stability at 1.5 A cm^{-2} in a PEM cell (80 ℃, ambient pressure). Reproduced with permission.[90] Copyright 2025, Springer Nature.

This facet-dependency has been well-documented in layered hydroxide systems. Zhu et al. demonstrated that the surface reconstruction of β-$Ni(OH)_2$ exhibits pronounced facet selectivity. After 1000 electrochemical cycles, an approximately 16 nm thick forms specifically at the (10$\bar{1}$0) edge facets (Fig. 10a), confirming the generation of $Ni_{1-x}O$ via surface reconstruction rather than deposition (Fig. 10b). The oxidation of β-$Ni(OH)_2$ into the catalytically active β-NiOOH phase, as well as the subsequent OER process, preferentially occurs on the edge facets (Fig. 10c).[88] Similarly, Xue et al. constructed a honeycomb-like cobalt hydroxide with abundant nanopores, enabling the selective anchoring of Fe species within the channels. DFT calculations reveal that, compared with the (0001) basal plane, Fe species exhibit significantly enhanced adsorption energies at the (10$\bar{1}$0) sites on the nanopore walls (Fig. 10d). Molecular dynamics (MD) simulations in Fig. 10e further demonstrate that these (10$\bar{1}$0)-based nanopores provide strong spatial confinement, effectively suppressing the diffusion and leaching of Fe active centers into the electrolyte.[89] A similarly decisive facet effect is observed in noble-metal catalysts. Taking IrO_2 as an example, theoretical studies indicate that the (101) facet delivers the lowest OER energy barrier, outperforming the (110) and (200) facets. Mechanistically, a downshift of the d-band center weakens the binding strength of oxygenated intermediates, rendering the

rate-determining step (RDS) the lower-barrier transformation of *OH to *O (Fig. 10f). Notably, IrO_2 (101) monolayers exhibit exceptional electrochemical durability, sustaining stable operation for over 10,000 h at a constant current density of 1.5 A cm^{-2} (Fig. 10g). These results highlight that rational selection and regulation of exposed facets can markedly enhance catalyst stability and extend operational lifetime.[90]

Atomic defect engineering is widely recognized as an effective strategy for the precise regulation of electronic structure and interfacial coordination environments. In particular, increasing the electron density around metal centers facilitates a reduction in the oxidation state of metal cations, thereby rendering intrinsic oxygen vacancies more effective in triggering structural reconstruction during catalytic reactions. Wang et al. employed multiple operando characterization techniques to probe the kinetics of the OER, revealing that oxygen vacancies can induce dynamic reconstruction in defective Co_3O_4. As shown by the cyclic CV curves in Fig. 11a, two oxidation peaks (A1 and A2) indicate that V_O-Co_3O_4 can be oxidized to CoOOH at potentials significantly lower than those required for pristine Co_3O_4. Combined electrochemical impedance spectroscopy (EIS) results in Fig. 11b demonstrate that the introduction of oxygen vacancies markedly accelerates OH^- adsorption, driving V_O- Co_3O_4 toward the formation of Co-OOH* intermediates, thereby promoting charge transfer and enhancing deprotonation capability. Furthermore, operando EXAFS measurements confirm that, compared with pristine Co_3O_4, the dynamic reconstruction of active species in V_O- Co_3O_4 occurs at substantially lower potentials (Fig. 11c).[91]

View Article Online
DOI: 10.1039/D6SC03869G

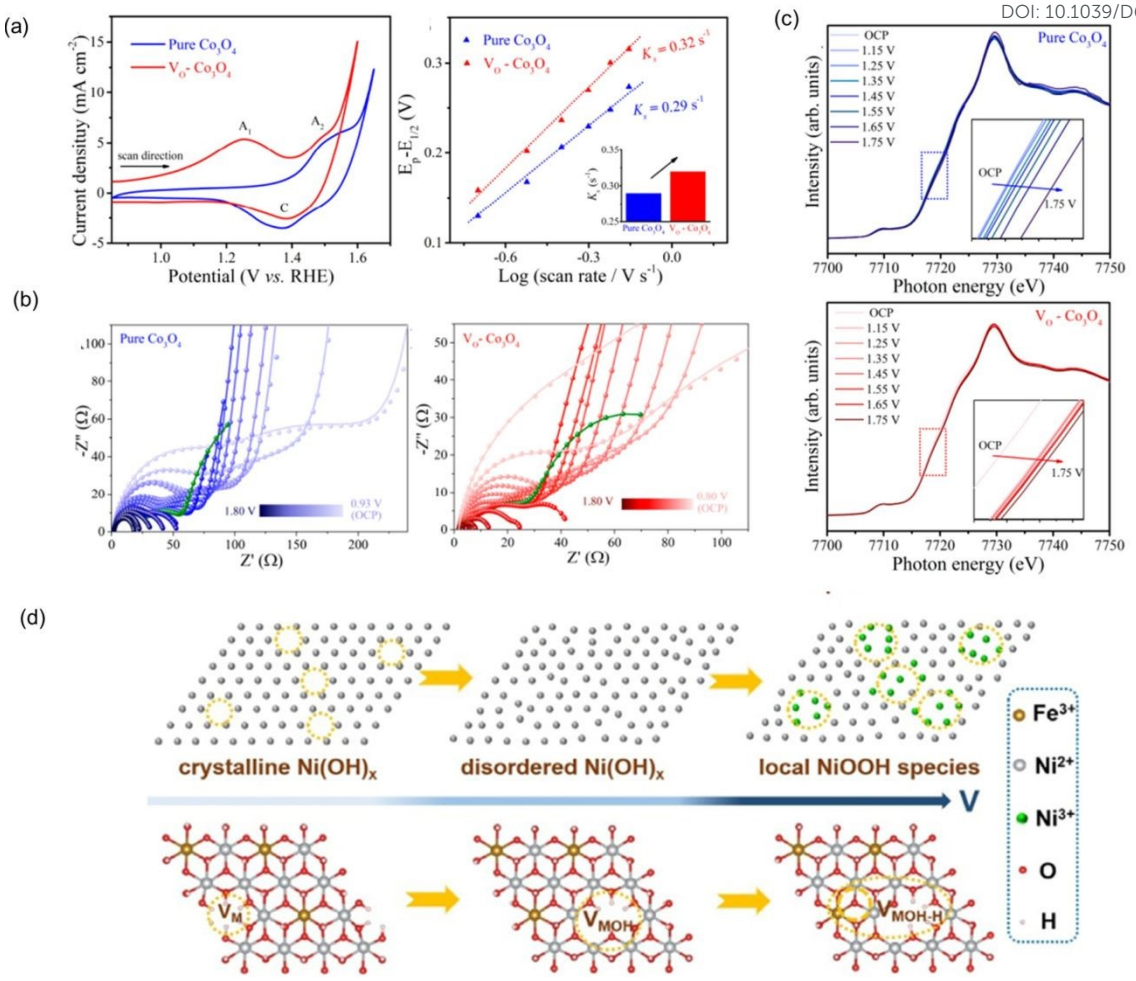

Fig. 11 (a) First cyclic CVs measured and Ks for Co_3O_4 and V_O-Co_3O_4 in 1 M KOH. (b) Nyquist plots for Co_3O_4 and V_O-Co_3O_4 catalysts at different potentials versus RHE in 1 M KOH. (c) Operando XAFS for Co K-edge of pure Co_3O_4 and V_O-Co_3O_4. Reproduced with permission.[91] Copyright 2020, American Chemical Society. (d) Schematic illustration of hydrogen atom loss (yellow dotted circle). Reproduced with permission.[92] Copyright 2021, Wiley.

Beyond oxygen vacancies, cation vacancies offer another powerful handle to modulate the intrinsic electronic structure, reconstruction dynamics, and electrocatalytic performance. Shi et al. precisely introduced Ni cation vacancies into spinel $NiFe_2O_4$, which significantly enhanced electrochemical surface reconstruction during the OER. Theoretical calculations further reveal that cation vacancies increase the octahedral Ni-O covalency in spinel nickel ferrite, lowering the barrier for surface reconstruction and promoting the in situ transformation into highly active oxyhydroxide phases under reaction conditions, leading to synergistically improved catalytic activity and stability.[93] In addition, Wu et al. demonstrated that V_M (M=Ni/Fe) cation-vacancy defects in NiFe-LDH can drive reconstruction of surface crystalline Ni(OH)x. As shown in Fig. 11d, the process proceeds progressively with increasing potential,

following a crystalline Ni(OH)x → disordered Ni(OH)x → local NiOOH species reconstruction pathway.[92]

3.1.2 Electronic Structure and Bonding Modulation

Heteroatom doping is widely used to tune the electronic structure and local chemical environment of catalysts, thereby regulating their reconstruction pathways and intrinsic stability. In particular, cation incorporation has been shown to promote the formation of highly active MOOH phases during the OER. Zhang et al. demonstrated via in situ Raman spectroscopy (Fig. 12a) that Ce doping in $Ce_{0.1}$-Fe_2P/NiCoP@NF significantly lowers the potential required for FeOOH formation compared with the undoped counterpart, confirming accelerated reconstruction kinetics, which is further supported by XPS evidence of partial Ce dissolution and phosphide-to-(oxy)hydroxide conversion (Fig. 12b).[94] Notably, under harsh acidic conditions, Kang et al. doped Ta into the RuO_2 lattice, significantly increasing the activation energy for Ru dissolution and enabling stable operation for up to 2800 h at an industrially relevant current density of 1 A cm^{-2} as shown in Fig. 12c.[95] Wei et al. demonstrated that Mo incorporation into RuO_2 induces weak Ru-Mo metallic bonding, which promotes electron transfer from Mo to Ru. This electronic interaction weakens the Ru-O_{bri} bonds, reduces Ru-O covalency, and thereby suppresses the LOM (Fig. 12d).[96]

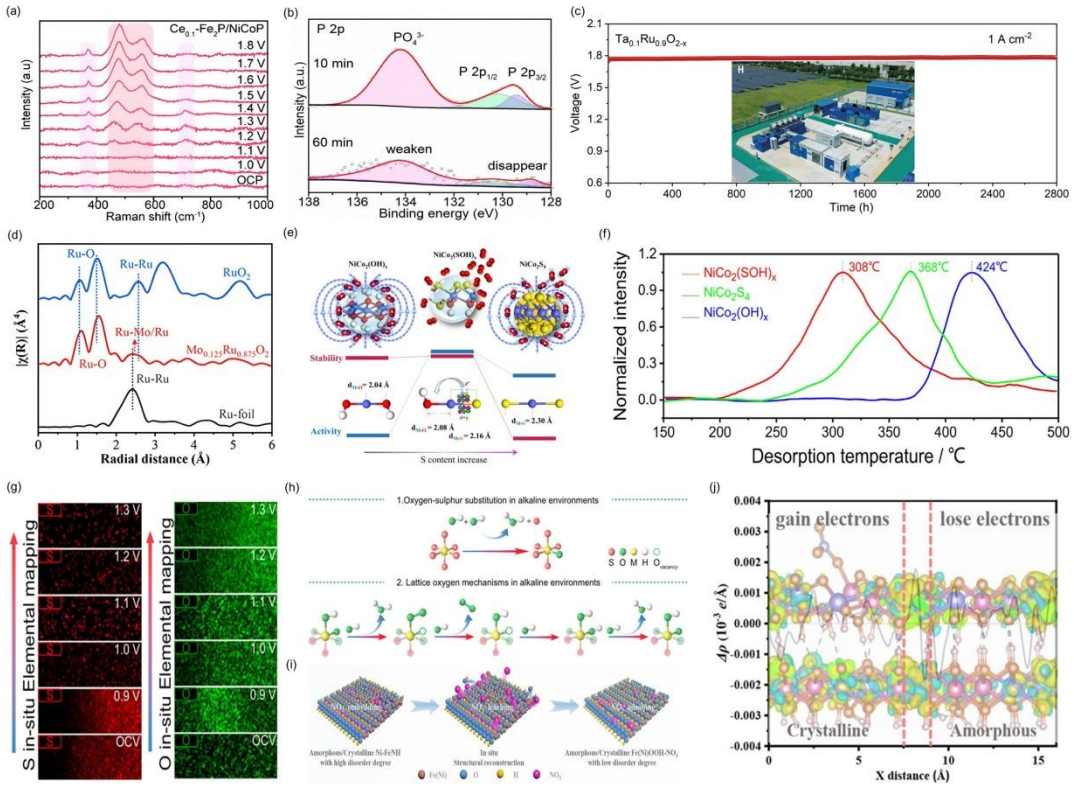

View Article Online
DOI: 10.1039/D6SC03869G

Fig. 12 (a) In situ Raman spectra of $Ce_{0.1}$-Fe_2P/NiCoP@NF in OER. (b) P 2p XPS spectra after 10 and 60 min of OER at 0.5 A cm^{-2}. Reproduced with permission.[94] Copyright 2025, Wiley. (c) Voltage-time curves of PEM-WE with $Ta_{0.1}Ru_{0.9}O_{2-x}$. Reproduced with permission.[95] Copyright 2025, American Association for the Advancement of Science. (d) FT-EXAFS spectra of $Mo_{0.125}Ru_{0.875}O_2$. Reproduced with permission.[96] Copyright 2025, Royal Society of Chemistry. (e) Ultimate unity of OER performance of $NiCo_2(S_xOH_{2-x})_y$. (f) O atoms TPD of $NiCo_2(OH)x$, $NiCo_2(SOH)_x$, and $NiCo_2S_4$. Reproduced with permission.[97] Copyright 2017, American Chemical Society. (g) In-situ elemental mapping of S and O. (h) Lattice oxygen mechanism with S-O substitution. Reproduced with permission.[68] Copyright 2023, Springer Nature. (i) Schematic reconstructed process of the crystalline phase in Ni FeNH. (j) Charge density difference analyses of NO_3^- adsorption on the Fe(Ni)OOH. Reproduced with permission.[98] Copyright 2025, Wiley.

Beyond cation doping, anion doping exhibits highly dynamic and structure-specific mechanisms in regulating catalyst stability. A representative example is the dual-ligand synergistic modulation strategy reported by Wei et al., in which sulfur and hydroxyl ligands were co-introduced into $NiCo_2(SOH)_x$ catalysts to completely solve the painful unity between the conflicted stability and activity issues of transition metal catalysts for OER (Fig. 12e). Dual-ligand coordination effectively tailors the electronic structure of the metal active centers, suppressing the paramagnetic character of the catalyst and thereby weakening the adsorption strength of the O_2 product with paramagnetism and facilitating the release of active sites (Fig. 12f).[97] In addition, sulfide-based systems typically undergo an electrochemically driven dynamic S-O exchange process during activation. Hu et al. revealed by in situ elemental mapping (Fig. 12g) that, in $(NiCo)S_{1.33}$, lattice sulfur atoms are partially substituted by oxygen from the electrolyte prior to the formation of reconstructed active species, resulting in a surface shell where lattice oxygen and sulfur coexist. This S-O exchange originates from the modulation of metal-sulfur coordination by specific Ni and Co occupancies, giving rise to a $(NiCo)O_xS_{1.33-x}$ surface structure. Such a transformation substantially lowers the energy barrier for converting sulfides into active oxygen/(oxy)hydroxide derivatives and increases the contribution of lattice oxygen to the catalytic process Fig. 12h.[68] To further enhance the stability of reconstructed phases, the incorporation of oxygen anions represents an effective strategy by improving their crystallinity. Using Ni-FeNH catalyst as an example, Wang et al. demonstrated that the leaching of NO_3^- induces the in situ formation of an ordered amorphous-crystalline heterojunction (NiOOH/FeOOH). This heterostructure, in synergy with anion modification, markedly enhances both catalytic activity and stability in Fig. 12i. DFT calculations reveal that NO_3^- preferentially migrates spontaneously from Ni to Fe sites to reduce adsorption energy, while charge analysis further indicates that electrons transfer from the

amorphous phase to crystalline Fe(Ni)OOH and are captured by surface NO_3^- species, thereby optimizing the interfacial electronic structure (Fig. 12j).[98]

Distinct from substitutional doping, interstitial doping has also achieved breakthrough progress in enhancing catalyst stability. Yin et al. electrochemically inserted Li into the interstitial sites of RuO_2, forming Li_xRuO_2 catalysts. Interstitial Li doping introduces additional Ru-O_{bri}-Li configurations, which establish an electron‐transfer pathway from Li to Ru and thereby effectively modulate the electronic structure of Ru active sites (Fig. 13a).[99] Building on this concept, Wei et al. further employed an ion-exchange resin strategy to incorporate highly corrosion-resistant Si atoms into the interstitial lattice sites of RuO_2, resulting in Si-RuO_2 catalysts. Similar to $LiRuO_2$, the interstitial Si doping also reduces the oxidation state of Ru and weakens the Ru-O covalency through the corresponding Ru-O_{bri}-Si configuration, which significantly suppresses over-oxidation of the Ru sites and LOM pathways (Fig. 13b,c). As a consequence, Si-RuO_2-0.1 requires an overpotential of only 226 mV at 10 mA cm^{-2} and maintains stable operation for over 800 h without noticeable activity decay (decay rate $\approx$ 52 $\mu V\ h^{-1}$).[100]

Beyond doping, alloy and defect engineering also provide powerful routes to tune the electronic configuration of catalysts. Alloy engineering involves incorporating one or more elements into the host lattice, generating synergistic electronic effects, lattice strain, and modified coordination environments.[101] These effects can shift the d-band center away from or toward the Fermi level, thereby optimizing the binding strength of key oxygen intermediates and improving OER kinetics. In particular, high-entropy alloys (HEAs) offer high electronic structure tunability. Song et al. reported that nanoporous ZnNiCoIrMn HEAs prepared through selective Zn removal exhibited redistributed electron density around Ir sites, which tailored the electronic structure of active Ir centers (Fig. 13d). The incorporation of Mn further modulated the Ir electronic structure and shifted the d-band center away from the Fermi level, thereby weakening the adsorption of reaction intermediates and facilitating the OER process (Fig. 13e,f).[102]Defect engineering can also optimize the adsorption behavior of intermediates by inducing lattice distortion or changing the coordination environment of active metal centers to alter local electron distribution. Wu et al. demonstrated that the introduction of surface oxygen vacancies into Rh-doped RuO_2 stabilized low-valent Ru centers and formed Ru-O-Rh active sites, enabling a lattice oxygen mediated mechanism-oxygen

vacancy site mechanism (Fig. 13g), thereby significantly enhancing acidic OER activity and stability (Fig. 13h).[103]

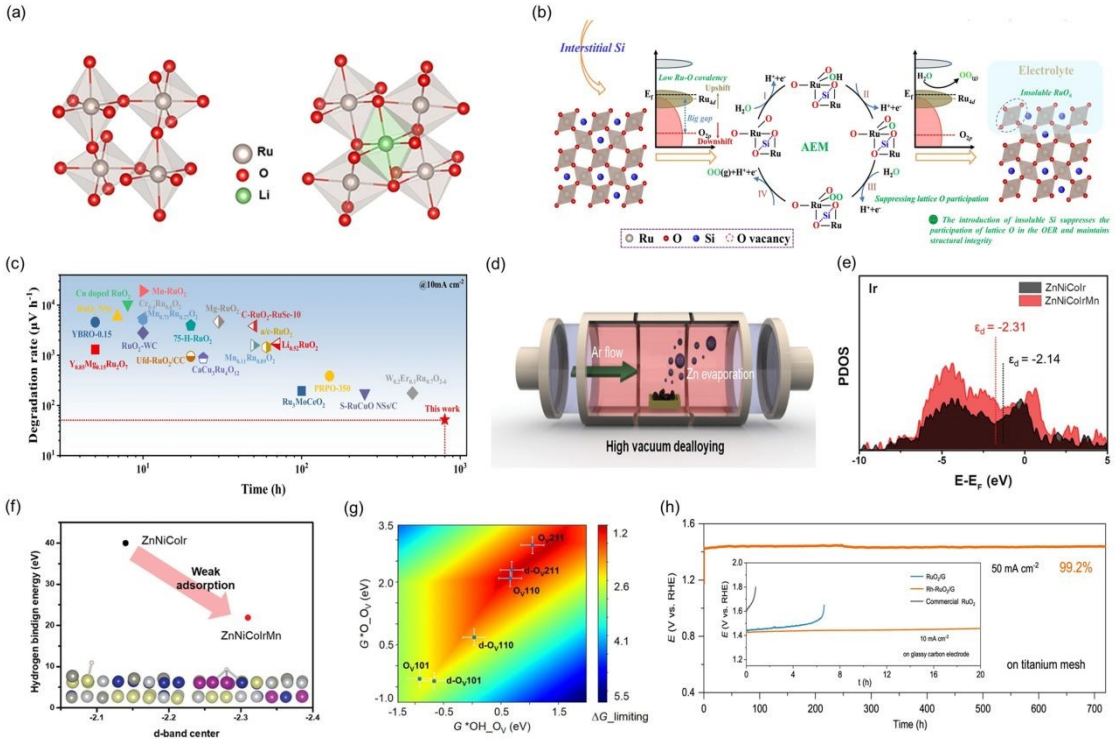

Fig. 13 (a) RuO_6 octahedron before and after lithium intercalation. Reproduced with permission.[99] Copyright 2022, Springer Nature. (b) Schematic diagram of the enhanced stability caused by interstitial Si doping. (c) Comparison of the stability and degradation rate of the Ru-based oxide catalyst at 10 mA cm^{-2}. Reproduced with permission.[100] Copyright 2024, Springer Nature. (d) Scheme of dealloying process of ZnNiCoIrMn. (e) d-band projected DOS (pDOS) of Ir for ZnNiCoIr and ZnNiCoIrMn. (f) Free energy diagram of ZnNiCoIrMn. Reproduced with permission.[102] Copyright 2023, Wiley. (g) A two-dimensional activity map for LOM-OVSM mechanism. (h) The galvanostatic curves at a current density of 10 mA cm^{-2} and 50 mA cm^{-2}. Reproduced with permission.[103] Copyright 2023, Springer Nature.

3.1.3 Interfacial Synergistic Stabilization

By coupling two or more materials with distinct compositions, crystal structures, or electronic properties, heterostructures can be constructed through interfacial interactions to form composite systems. Beyond introducing additional active components, heterointerfaces precisely induce favorable catalyst reconstruction, forming thermodynamically more stable active phases and thereby optimizing reaction pathways while enhancing structural stability.

Support-induced heterostructural reconstruction can alter the reaction mechanism and fundamentally suppress lattice corrosion. For example, Zou et al. demonstrated that using TiOx@Ti as a substrate can drive Ir to undergo an unusual bulk phase transformation under electrochemical conditions, producing crystalline rutile IrO_2 in

Fig. 14a. This substrate-guided crystallization process shifts the OER pathway from the LOM, which is prone to lattice oxygen loss and structural collapse, to the more stable AEM (Fig. 14b).[64] Similarly, Li et al. demonstrated that the Ni-BPM system exhibits reversible self-reconstruction during activation to form a γ-NiOOH/Ni-BPM heterostructure, such reversible structural evolution significantly enhances tolerance to the harsh OER environment.[104]

Moreover, heterointerfaces can induce interfacial electron transfer by exploiting differences in electronegativity between constituent components, thereby tuning the adsorption strength of key oxygenated intermediates and stabilizing otherwise labile components beyond their intrinsic stability limits. This interfacial regulation provides a viable route to break free from the traditional shackles of the activity-stability trade-off.[105, 106] Sun et al. reported a Ni_3S_2-CeO_2 heterostructure in which strong interfacial electronic interactions induced charge redistribution between Ni and Ce species, as evidenced by the negative shift of the Ni 2p peaks and the increased Ce^{4+} fraction in the Ce 3d spectra (Fig. 14c). Meanwhile, the interfacial electronic coupling further strengthened the adsorption of key oxygenated intermediates, including *OH, *O, and *OOH (Fig. 14d), thereby enhancing the OER catalytic activity.[107] Similarly, Yang et al. reported an IrO_2/MoS_2/CNT heterostructured catalyst as a representative platform to illustrate interfacial electronic structure regulation. XPS results showed pronounced positive shifts of both the Ir 4f and Mo 3d signals in IrO_2/MoS_2/CNT (Fig. 14e), evidencing strong electronic interactions at the IrO_2-MoS_2 interface and confirming the formation of a well-defined heterojunction. Band structure analysis further revealed the establishment of an n-n type heterojunction, where the built-in electric field enables interfacial carrier redistribution (Fig. 14f). Such interfacial regulation optimizes the adsorption energetics of oxygenated intermediates at Ir sites while concurrently suppressing IrO_2 over-oxidation and dissolution, thereby reconciling enhanced catalytic activity with improved durability in overall water splitting.[108]

View Article Online
DOI: 10.1039/D6SC03869G

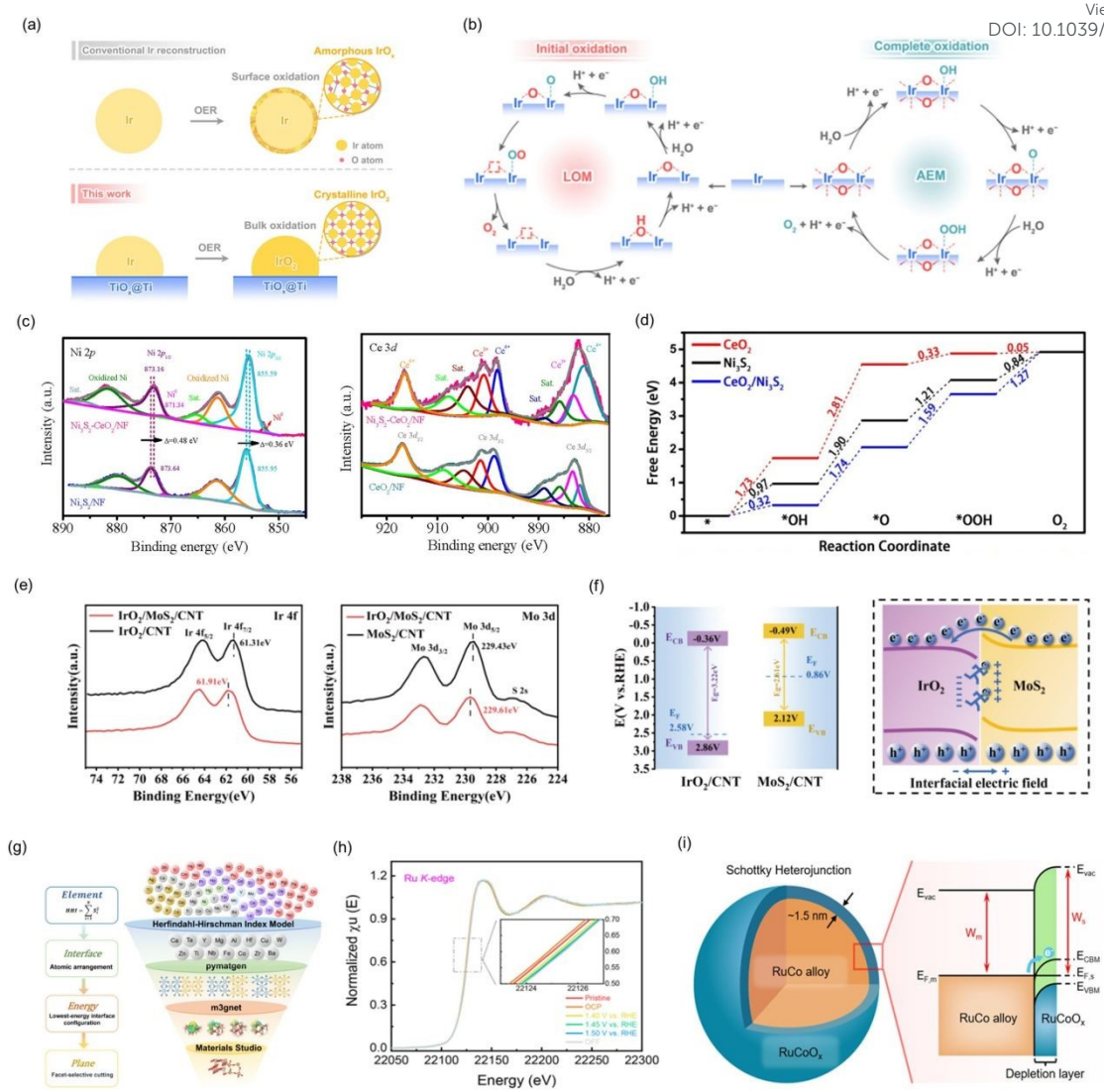

Fig. 14 (a) Schematic diagram of electrochemically induced reconstruction of Ir nanoparticles. (b) Schematic illustration of LOM and AEM for oxidized Ir/TiOx@Ti. Reproduced with permission.[64] Copyright 2025, Springer Nature. (c) XPS spectra in the Ni 2p and Ce 3d regions. (d) Calculated free energy diagrams for OER. Reproduced with permission.[107] Copyright 2021, Elsevier. (e) XPS spectra of Ir 4f and Mo 3d. (f) Energy band alignment of IrO_2/CNT and MoS_2/CNT, and schematic illustration of the interfacial electronic structure in the IrO_2/MoS_2/CNT heterojunction. Reproduced with permission.[108] Copyright 2025, American Chemical Society. (g) A schematic illustration of the multi-step rational screening-guided process for high-melting-point metal oxide protective layers. (h)The Ru K-edge XANES spectra measured in acidic solution under pristine, OCP. Reproduced with permission.[109] Copyright 2025, Wiley. (i) Schematic illustrations of the core/shell RuCo/RuCoOx nanospheres and the Schottky heterojunction in RuCo/$RuCoO_x$. Reproduced with permission.[110] Copyright 2024, American Chemical Society.

Under reaction conditions, heterointerfaces can act as protective layers by isolating active phases from harsh electrochemical environments, thereby suppressing dissolution and over-oxidation. Ma et al. identified Ta-based oxides as optimal protective shells for RuO_2 in acidic OER through multistep theoretical screening (Fig. 14g). Guided by this prediction, a core-shell RuO_2@TaO_x catalyst was constructed, and

in situ Quick-XAS (Fig. 14h) confirmed that Ru remains the active site while Ta suppresses Ru over-oxidation, with the amorphous TaO_x shell effectively inhibiting RuO_2 dissolution and enhancing durability.[109] Similarly, Liu et al. reported that an ultrathin and conformal depletion layer at a $RuCo/RuCoO_x$ core/shell heterojunction forms a Schottky-type heterointerface, where the depletion layer serves as a physical and chemical barrier that effectively isolates active Ru sites from the harsh electrochemical environment (Fig. 14i). This protective interface effectively stabilized the oxidation state of active sites during operation, thereby suppressing over-oxidation and mitigating dissolution, while preserving the catalytic activity under acidic conditions. Such an intrinsic protective interface stabilizes the oxidation state of active sites during operation, thereby suppressing over-oxidation and mitigating dissolution while preserving high catalytic activity under acidic conditions.[110]

3.2 Enhancing the Dynamic Stability of OER Electrocatalysts

Distinct from static catalysts designed for intrinsic stability, many high-performance OER electrocatalysts are not structurally invariant under operating conditions, but instead undergo dynamic, reversible, or irreversible structural evolution. Understanding and harnessing these dynamic transformations, therefore, represents an important and complementary strategy for enhancing catalyst stability.

3.2.1 Electrocatalyst Activation

Electrochemical activation is an effective strategy widely employed to induce structural evolution of pre-catalysts. Xu et al. realized the delithiation of $LiNiO_2$ through electrochemical cycling, accompanied by its transformation into highly active NiOOH that serves as the real catalytic site for the OER. As illustrated in Fig. 15a, a NiOOH layer preferentially forms on the surface, while Ni species migrate toward the surface, assisted by electrochemical delithiation, leading to the contraction of Ni-O bonds. Electron energy loss spectroscopy (EELS) and XAS characterizations reveal that Ni migrates to the surface, forming low-coordination NiOO* species and inducing surface reconstruction, thereby enhancing catalytic activity (Fig. 15b). As shown in Fig. 15c, the OER current density of $LiNiO_2$ continuously increases during the first 500 cycles but gradually decreases from 500 to 1000 cycles, indicating that the number of activation cycles exerts a double-edged effect on OER performance and must be carefully optimized during electrochemical activation.[111]

View Article Online
DOI: 10.1039/D6SC03869G

Beyond cycling number, surface reconstruction of catalysts is also highly dependent on the applied potential. During potential scanning, the catalyst surface undergoes multiple redox transitions, with surface reconstruction becoming particularly pronounced under OER conditions. Zhou et al. monitored the Raman spectra in the potential range of 1.23-1.45 V vs. RHE (Fig. 15d). The results reveal potential-dependent and fully reversible Raman evolution, demonstrating the reversible surface reconstruction of manganese oxybromides (MOB). Notably, the introduction of Ru single atoms markedly promotes the reversible transformation of MOB into γ-MnO_2 under OER conditions and lowers the onset potential for reconstruction by approximately 100 mV.[112] In addition, Huang et al. found that by tuning the potential window during continuous cycling, partial Te leaching occurs at low potentials, while surface Ir is further oxidized to IrO_x at higher potentials (Fig. 15e).[113]

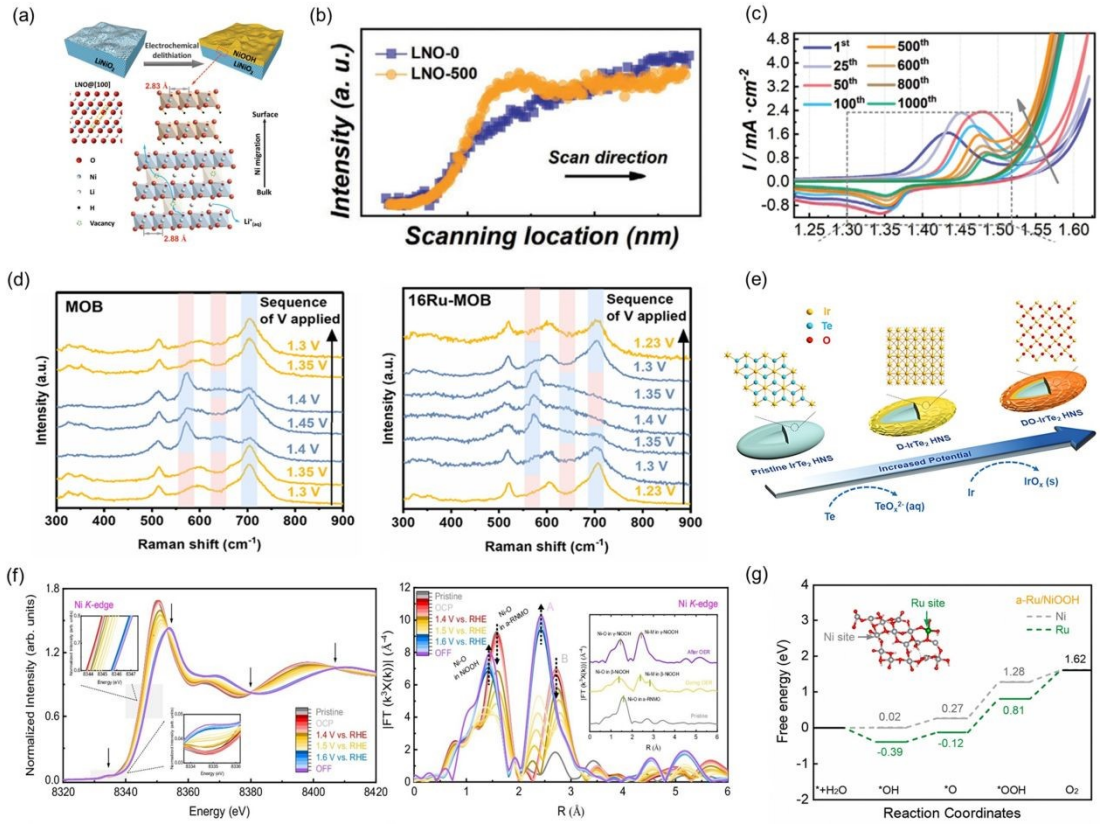

Fig. 15 (a) The schematic diagram of the evolution of $LiNiO_2$ in electrochemical process. (b) Extracted line-profiles for Ni confirmed the Ni intensity of LNO-500 on the surface is more than LNO-0, suggesting that Ni migrates to the surface under the OER process. (c) CV at a scan rate of 10 mV s^{-1} in O_2-saturated 1 m KOH (99.999%) showing the current per geometric area for the different cycles for $LiNiO_2$ (LNO) catalyst. Reproduced with permission.[111]Copyright 2020, Wiley. (d) In situ Raman spectra obtained with systematically applied potential around the transition voltage for MOB and 16Ru-MOB. Reproduced with permission.[112] Copyright 2025, American Chemical Society. (e)Schematic diagram of formation of $IrTe_2$ HNSs with metal Ir shell and IrO_x surface (D-$IrTe_2$ and DO-$IrTe_2$, respectively) via electrochemical dealloying. Reproduced with permission.[113] Copyright 2020, Wiley.

View Article Online
DOI: 10.1039/D6SC03869G

(f) Ni K-edge XANES spectra and the magnitude of the Fourier transform for the Ni K-edge EXAFS spectra of a-RNMO measured in 1 M KOH under pristine, OCP, OER operating conditions (1.4, 1.5, and 1.6 V vs. RHE), and OCP after OER operation. (g) Gibbs free energy diagram of the OER process on a-Ru/NiOOH (U = 0 V). Reproduced with permission.[114]

Furthermore, surface activation can enhance catalytic performance by inducing the formation of amorphous oxides, which provide more diverse coordination environments and abundant active sites. Ma et al. employed millisecond-resolved operando Quick-XAS combined with in situ Raman spectroscopy to capture the stepwise reconstruction of Ni species, the rapid dissolution of Mo, and the dynamic formation of the NiOOH active phase (Fig. 15f). This work reveals a "complementary amorphous-electronic modulation mechanism" arising from the synergistic interaction between the amorphous substrate and Ru single atoms. Specifically, amorphous $NiMoO_x$ offers a flexible and open framework that exposes abundant active sites, while Ru single atoms optimize the adsorption of *OH/*O intermediates via electronic redistribution, thereby synergistically enhancing catalytic activity and stability (Fig. 15g). These findings demonstrate that electrochemical activation enables amorphous oxides to guide reversible surface reconstruction, achieving a balance between high catalytic activity and stability.[114]

3.2.2 Surface Reconstruction and Stable Formation of Active Phases

Extensive studies have shown that many transition metal compounds undergo in situ phase transformation under OER conditions, forming new oxide or oxyhydroxide phases. These reconstructed species are generally better adapted to the OER environment, thereby exhibiting enhanced structural stability and sustained catalytic activity during long-term operation.

Wei et al. employed a self-terminating electrochemical surface reconstruction strategy to activate spinel $Co_2Fe_{0.25}V_{0.75}O_4$, enabling outstanding OER performance in alkaline electrolytes. XPS analysis (Fig. 16a) revealed that Fe substitution at V sites during anodic OER shifts the bulk O 2p band upward, thereby inducing abundant surface oxygen vacancies and promoting lattice oxygen oxidation. Specifically, Fe incorporation optimizes the pre-oxidation state of Co and enhances Co-O covalency, while selective V leaching accelerates surface reconstruction to form CoOOH active species (Fig. 16b). This study clearly demonstrates that the reconstructed CoOOH phase is the true catalytically active species for OER and can remain stably anchored on the electrode surface during prolonged electrolysis, thus endowing the catalyst with

sustained activity.[115] Similarly, Patzke et al. developed Fe-doped cobalt cyanamide ($Co_{0.67}Fe_{0.33}NCN$) nanoparticles as efficient OER precatalysts, maintaining a stable overpotential for at least 290 h. Combined in situ XAS, XRD, and post-reaction analyses revealed an initial amorphization below 1.4 V (vs RHE), followed by oxidation of the metal centers and the formation of metal (oxy)hydroxide phases above 1.45 V (vs RHE). Structural defects in the low-crystalline samples accelerate irreversible surface reconstruction during OER, promoting the formation of high-valence γ-$Co_xFe_{1-x}OOH$ species (Fig. 16c,d). These reconstructed (oxy)hydroxides were identified as the true active phases for OER, providing a structural basis for simultaneously achieving high activity and long-term stability.[116] In addition, Fan et al. demonstrated that the introduction of dual-anion defects and amorphous phases facilitates rapid and deep reconstruction, leading to the formation of stable $Co_{0.7-x}Fe_{0.3-y}P/Co_xFe_yOOH$ active phases and activating the lattice oxygen mechanism (LOM). Consequently, the OER proceeds through a combined LOM and conventional adsorbate evolution mechanism (AEM), effectively balancing catalytic activity and structural stability (Fig. 16e).[117]

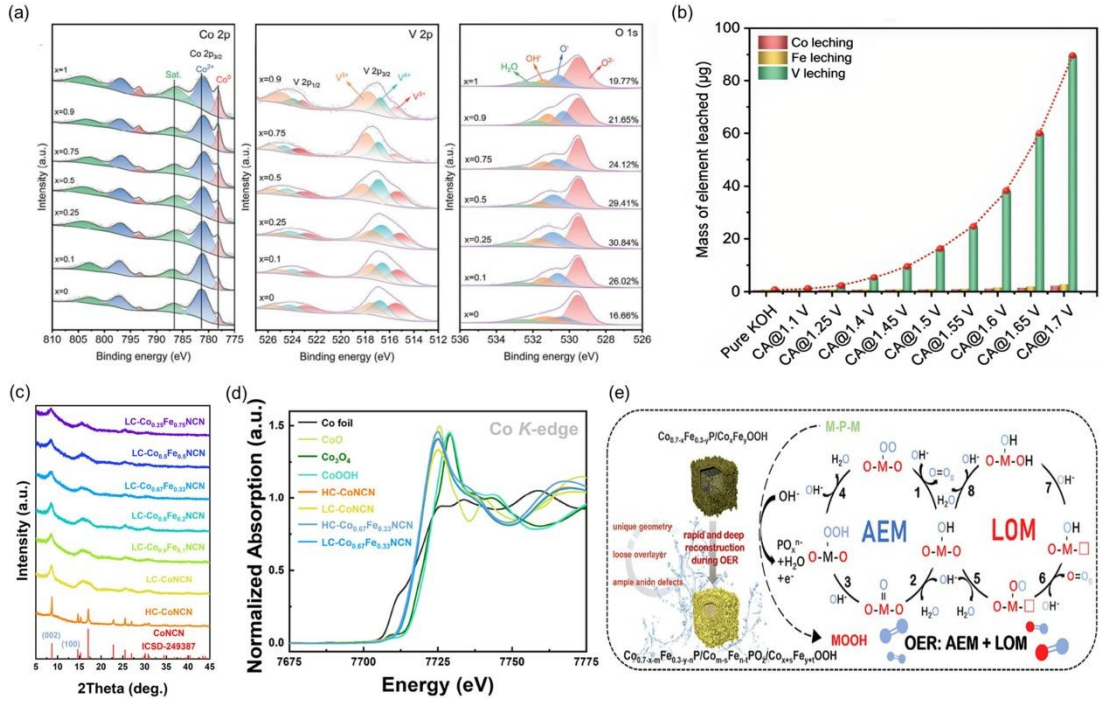

Fig. 16 (a) High-resolution XPS spectra of Co 2p, V 2p, and O 1s for $Co_2Fe_xV_{1-x}O_4$. (b) Cumulative amounts of elements leached after consecutive series of chronoamperometry (CA) for $Co_2Fe_{0.25}V_{0.75}O_4$. Reproduced with permission.[115] Copyright 2024, Wiley. (c) PXRD pattern of $Co_xFe_{1-x}NCN$. (d) Co K-edge XANES spectra of HC-/LC-CoNCN and HC-/LC-$Co_{0.67}Fe_{0.33}NCN$ and reference Co compounds. Reproduced with permission.[116]Copyright 2025, American Chemical Society. (e) The proposed OER mechanism on $Co_{0.7-x}Fe_{0.3-y}P/Co_xFe_yOOH$. Reproduced with permission.[117] Copyright 2025, Wiley.

View Article Online
DOI: 10.1039/D6SC03869G

Based on these advances, surface reconstruction is increasingly regarded as a necessary and beneficial intermediate process. Accordingly, rational strategies that stabilize reconstructed active phases while suppressing their further transformation or degradation have emerged as effective routes to enhancing OER durability. This can be achieved either by precursor structure engineering to directly form the desired active phase upon reconstruction, or by elemental doping and defect engineering to modulate electronic states and metal-oxygen bonding, thereby preventing conversion into less active or soluble species. Overall, the shift from suppressing reconstruction to guiding and stabilizing reconstructed active phases offers a clear and generalizable pathway toward OER electrocatalysts with both high activity and long-term reliability.

3.2.3 Dynamic Equilibrium Regulation

During the OER, catalyst surfaces exist in a dynamic equilibrium involving dissolution and redeposition, as well as oxidation and reduction. Catalyst deactivation often arises from disruption of this balance, leading to net loss of active components or the formation of detrimental phases. Rather than attempting to completely suppress these dynamic processes, a more forward-looking strategy is to actively regulate external conditions to establish and sustain a dynamic equilibrium that favors both activity and stability, or even to harness this process for in situ renewal and self-repair of the catalytic interface.

Li et al. revealed that NiFe-based catalysts can achieve self-repair ability in alkaline media through a dynamic Fe exchange equilibrium between the catalyst and the electrolyte during OER, providing a compelling illustration of this concept. When the concentration of Fe leached from NiFe catalysts into the electrolyte reaches an appropriate level, a sufficient amount of Fe species can readsorb onto the reconstructed NiFe oxyhydroxide surface, thereby establishing a balance between repair and loss rates. This dissolution-readsorption process was directly verified by multiple experimental techniques. XPS analysis (Fig. 17a) demonstrated that the surface Fe signal of NiFe-LDH did not decrease noticeably after cycling; instead, the Fe/(Ni+Fe) ratio even increased slightly, suggesting that Fe dissolution does not simply lead to deactivation but instead participates in subsequent interfacial reconstruction. Furthermore, quantitative comparison of repair and loss rates (Fig. 17b) further confirmed that NiFe-LDH resides in a critical stability regime where the repair rate approximately equals the loss rate, enabling a dynamic self-repair steady state under OER conditions. As illustrated schematically in Fig. 17c, the stability of NiFe-based OER electrocatalysts

originates not from "resistance to dissolution" but from a dynamic self-repair equilibrium between Fe leaching and readsorption.[118] Consistently, Fan et al. demonstrated that regulating the Fe^{3+} concentration in the electrolyte can drive a dynamic interfacial equilibrium. Under alkaline conditions, trace Fe^{3+} markedly enhances the OER activity and stability of Ni-based catalysts by forming an active FeOOH/Ni interface in situ (Fig. 17d). At higher anodic potentials, FeOOH partially dissolves, establishing a reversible formation and dissolution balance. Precise control of Fe^{3+} concentration sustains active FeOOH while preventing excessive dissolution, thereby maintaining a stable and highly active catalytic interface (Fig. 17e,f).[119]

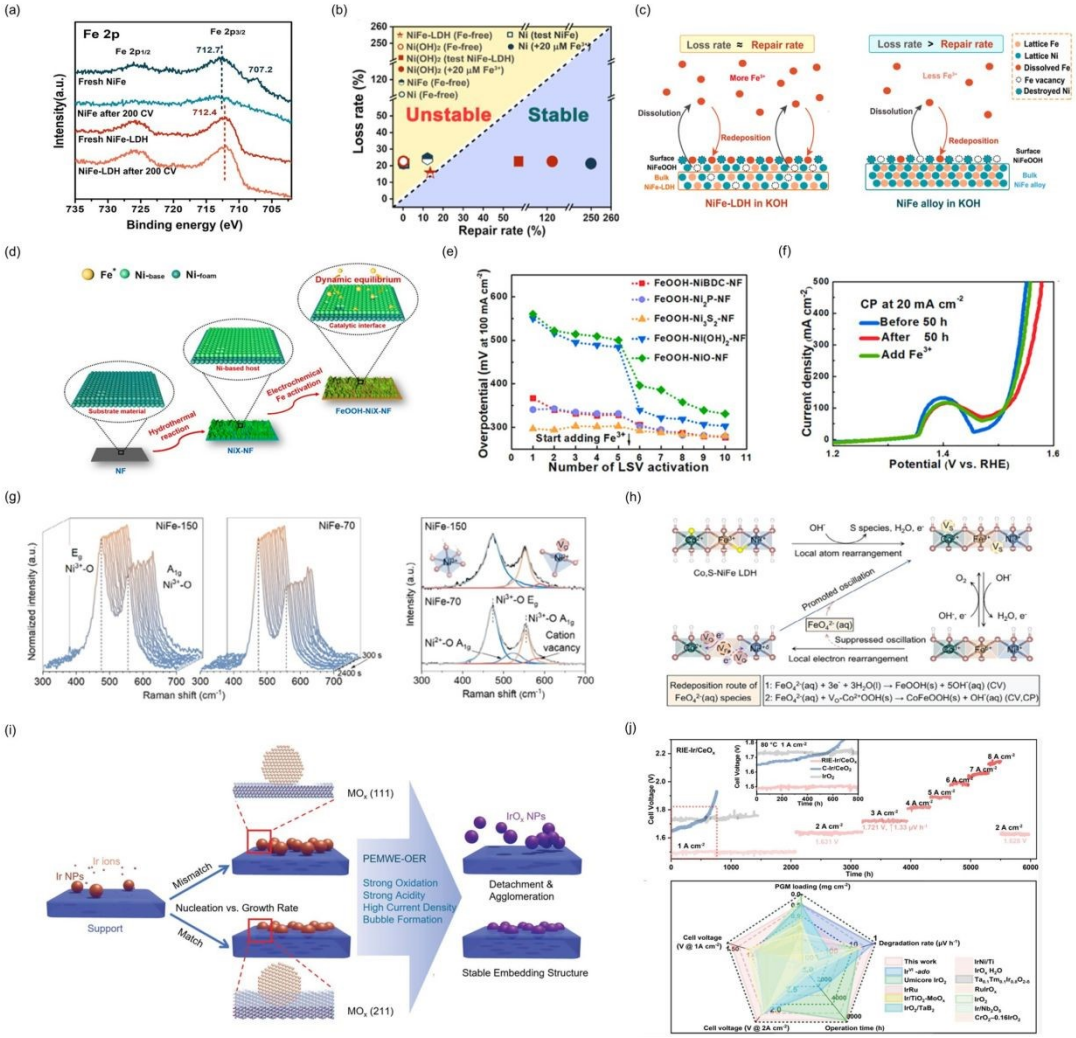

Fig. 17 (a) Fe 2p XPS spectra for the NiFe alloy and NiFe-LDH before and after 200 CV cycles. (b)Loss rate and repair rate of the activity at 1.7 V for various electrodes. (c) Schematic diagram of the Fe dissolution and redeposition for NiFe alloy and NiFe-LDH in KOH during the OER process. Reproduced with permission.[118] Copyright 2023, American Chemical Society. (d) Schematic illustration of synthesis of FeOOH-Ni-base on Ni foam. (e)The relationship between the number of electrochemical activation and the overpotential of different catalysts. (f) The LSV of FeOOH-NiBDC-NF before and after CP test at 20 mA cm^{-2}. Reproduced with permission.[119] Copyright 2022, Elsevier. (g) Operando Raman spectra of NiFe-70 and NiFe-150, normalized to the Eg intensity, and

corresponding fitted Raman spectra collected at 300 s. (h) Schematic illustration of the dynamic oscillation manners of NiFe LDH tuned by Co and S co-doping. Reproduced with permission.[120] Copyright 2025, Wiley. (i) Schematic illustration of the embedding strategy. (j) Chronopotentiometry of PEMWE with RIE-Ir/CeO_x at sequential current density and comparison with other Ir-based PEMWE-OER catalysts. Reproduced with permission.[121] Copyright 2025, American Association for the Advancement of Science.

Furthermore, Zhai et al. employed atomic-layer NiFe-LDH catalysts as a model system to elucidate the critical role of reversible structural oscillations in OER stability. By combining operando XAS and Raman spectroscopy with cyclic voltammetry and chronopotentiometry, it was demonstrated that surface atomic configurations directly govern the dynamic oscillatory behavior of local [Ni-O_2-Fe] active units under operating potentials (Fig. 17g). Through S and Co co-doping was demonstrated that in situ S leaching alleviates lattice mismatch and suppresses Fe dissolution, while electron-withdrawing Co provides favorable redeposition sites for Fe. This synergistic regulation enables reversible oscillation of local [Ni/Co-O_2-Fe] units and underpins the dynamic stability of the catalyst (Fig. 17h).[120] Importantly, the rate relationships between the evolution of the support structure and the nucleation of active metal species, catalytic systems can achieve self-stabilization during reactions. Zhang et al. exploited the ripening process of nanocrystals under sonication and heating, constructing a matching rate between the support growth rate and the catalyst nucleation rate (Fig. 17i). They embedded IrO_x nanoparticles into a ceria support, forming a stable and efficient supported catalyst, which significantly enhanced both the catalytic efficiency and stability (Fig. 17j).[121]

The elegance of these concepts lies in balancing the rates of dissolution and redeposition at the catalytic interface, as well as synchronizing the kinetic relationship between the support architecture and the nucleation behavior of active metal species. Thereby endowing OER electrocatalysts with a capacity for continuous self-repair rather than relying on static structural stability. This paradigm of dynamic regulation offers a new perspective and viable solution for addressing catalyst durability under harsh conditions, particularly for catalytic systems with intrinsically limited structural stability.

3.3 Regulation of Electrochemical and Operational Conditions

In practical industrial water electrolysis, electrode interfaces are continuously exposed to multiple dynamic challenges, including potential fluctuations, pronounced local pH variations, chemical corrosion by highly concentrated dissolved oxygen, and

mechanical stresses induced by gas bubble evolution. As discussed above, intrinsic material design alone is insufficient to fulfill the stringent stability requirements under industrially relevant conditions. Therefore, this section focuses on dynamic optimization of operating conditions can synergistically enhance the stability of the OER process.

3.3.1 Interfacial Microenvironment Regulation

Catalysts do not operate under vacuum conditions; instead, electrochemical reactions occur at the electrode/electrolyte interface, a typical solid-liquid interface. The ionic composition of the electrolyte, the local pH, and externally applied physical fields collectively define the interfacial microenvironment that dictates catalyst stability，rendering microenvironment engineering a powerful route toward industrially relevant durability.[122]

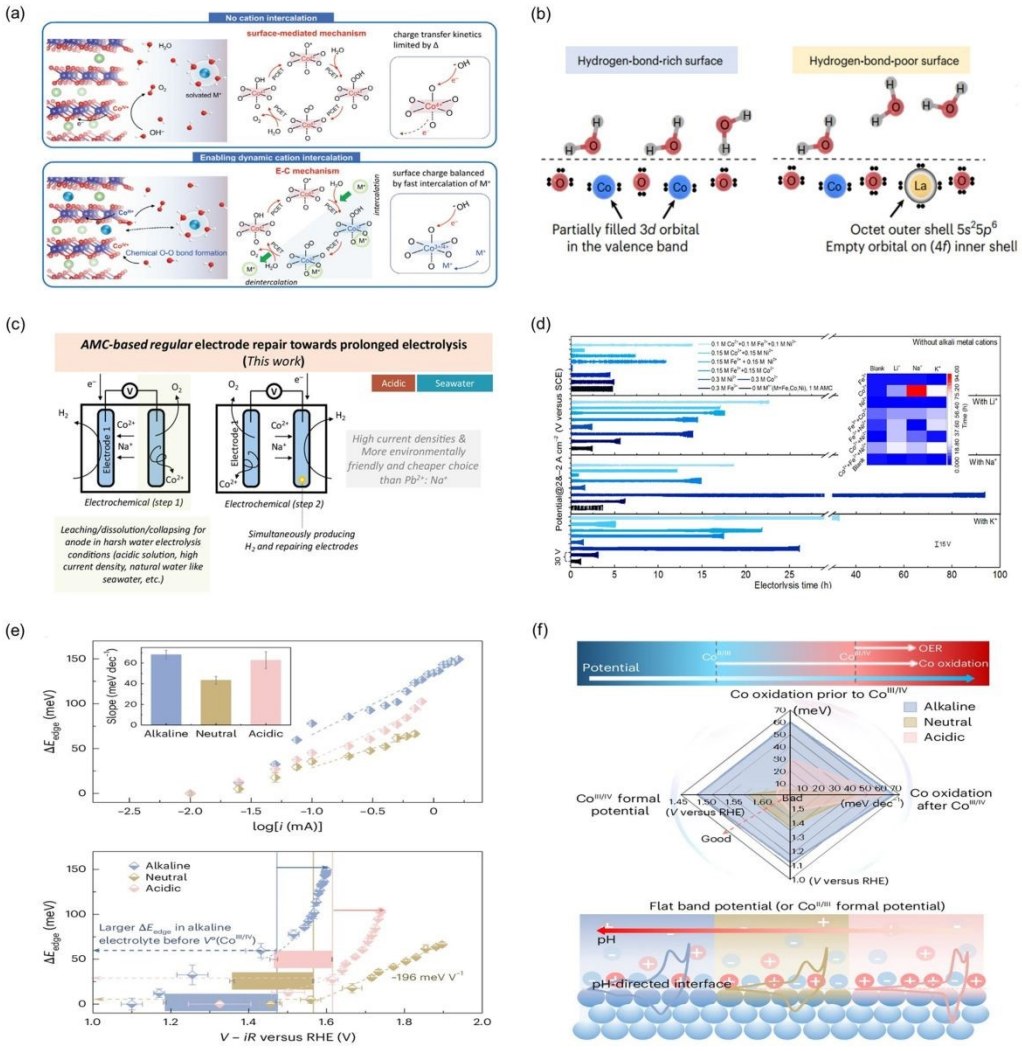

View Article Online
DOI: 10.1039/D6SC03869G

Fig. 18 (a) Schemata of surface-mediated reaction without cation intercalation and electrochemical-chemical (EC) mechanism with charge balanced by reversible cation (M^+) intercalation. Reproduced with permission.[123] Copyright 2025, Wiley. (b) Schematic illustration of water molecules on Co_3O_4 and lanthanum-dispersed Co_3O_4 surfaces. Reproduced with permission.[124] Copyright 2026, Springer Nature. (c) An AMC-based electrolysis scheme for electrode self-repair under harsh electrolysis conditions. (d) Alternating electrolysis with Fe-group ions and different alkali metal cations (AMCs). Reproduced with permission.[125] Copyright 2024, Springer Nature. (e) The ΔE_{edge} of the Co K edge, collected during CP measurement in a flow cell, is plotted as a function of log(i) and applied potential. (f) Summary of different parameters that contribute to the pH dependency of OER activity. Reproduced with permission.[126] Copyright 2025, Springer Nature.

Alkali metal cations in the electrolyte influence the structure of interfacial water through noncovalent interactions. Yang et al. investigated the incorporation of alkali cations (Li^+, Na^+, K^+, and Cs^+) into layered $LiCoO_2$ lattices and found that larger cations, such as Cs^+, disrupt the rigid interfacial water network, thereby facilitating water dissociation and stabilizing reaction intermediates. This effect indirectly lowers the overpotential required to trigger lattice oxygen evolution, leading to enhanced intrinsic stability (Fig. 18a).[123] Similarly, Görlin et al. employed in situ X-ray absorption spectroscopy to demonstrate that, for Ni-Fe-based catalysts, OER activity exhibits a pronounced dependence on electrolyte pH in the presence of alkali metal cations.[127] Furthermore, regulation of the interfacial microenvironment has been extended to the direct interactions between water molecules and catalyst surfaces. Peng et al. prepared a lanthanum and calcium co-doped Co_3O_4 catalyst, in which the introduction of weakly hydrophilic La creates atomic sites with specific water-molecule interactions (CoLa-SWMI). The CoLa-SWMI sites reconstruct the interfacial water environment and moderately alleviate the polarization of metal-oxygen bonds induced by hydrogen bonding with water molecules, thereby significantly extending the catalyst lifetime (Fig. 18b).[124] Beyond modulating interfacial water, alkali metal cations facilitate interfacial self-repair during alternating electrolysis. Sun et al. proposed an alternating electrolysis strategy that enables periodic in situ electrode repair through the synergistic interaction between Fe-group metal ions and alkali metal cations in the electrolyte. In particular, the unique Co^{2+}-Na^+ combo promotes the rapid and uniform deposition of a protective Co-containing layer during the hydrogen evolution stage, while the repeated deposition-dissolution process during alternating HER/OER operation enables prolonged electrolysis (Fig. 18c). As a result, Ni foam can operate stably for 93.8 h at ±2 A cm^{-2} (Fig. 18d), significantly prolonging electrode lifetime under harsh electrolysis conditions.[125]

View Article Online
DOI: 10.1039/D6SC03869G

However, the complexity of the interfacial microenvironment extends far beyond this. During highly gas-evolving reactions such as the OER, the local pH at the catalyst surface can deviate substantially from that of the bulk electrolyte. This local pH is governed by the buffering capacity of the electrolyte, ion transport kinetics, and the rates of water dissociation and formation, resulting in substantial dynamic fluctuations. Such local pH shifts often drive catalysts out of their Pourbaix stability windows, thereby triggering corrosion and structural deactivation. Using dynamic operando XAS in Fig. 18e, Fabbri et al. tracked the evolution of (hydro)oxide/electrolyte interfaces under different pH-directed conditions and revealed a strong dependence of the oxidation state and coordination environment of Co-based catalysts on local pH. The magnitude of the Co K-edge energy shift (ΔE_{edge}) showed marked pH dependence, being largest under alkaline conditions, intermediate in acidic media, and smallest near neutral pH consistent with the attenuated potential-driven Co oxidation under neutral conditions (Fig. 18f). These findings underscore the critical importance of maintaining interfacial pH homeostasis for regulating the evolution of catalytically active phases.[126]

Overall, tuning the electrolyte buffering capacity or introducing specific functional groups to anchor the local pH is an effective strategy to suppress acidic corrosion and excessive oxidation. Moreover, external physical fields, such as magnetic or localized thermal fields, can enhance bubble detachment and ion transport, thereby alleviating local overpotential buildup and interfacial microenvironment degradation under mass-transport limitations.

3.3.2 Dynamic Operation Regulation

Under practical operating conditions, such as frequent start-stop cycles, low-load operation, and rapid fluctuations in input power, continuous transient variations in anodic potential, cause the electrodes to operate under long-term nonequilibrium conditions. Load variations often lead to delayed responses between ion transport and reaction kinetics, resulting in concentration polarization, overpotential accumulation, and irreversible reconstruction of active phases.

Therefore, controlled regulation of transient operating states has become an important strategy for improving system stability. Open circuit potential (OCP) decay transients allow rapid capacitive discharge and gradual interfacial re-equilibration after current interruption, which may alleviate excessive polarization and maintain a more stable electrochemical microenvironment.[128] In addition to operational-state regulation, dynamic electrical input strategies have also been used to improve interfacial mass

transfer. Pulsed current or voltage can periodically perturb the electrical double layer (EDL), thereby promoting ion diffusion, alleviating concentration polarization, and improving charge-transfer kinetics (Fig. 19a). High-frequency pulse conditions further reduce electrochemical impedance and enhance hydrogen evolution efficiency.[129]

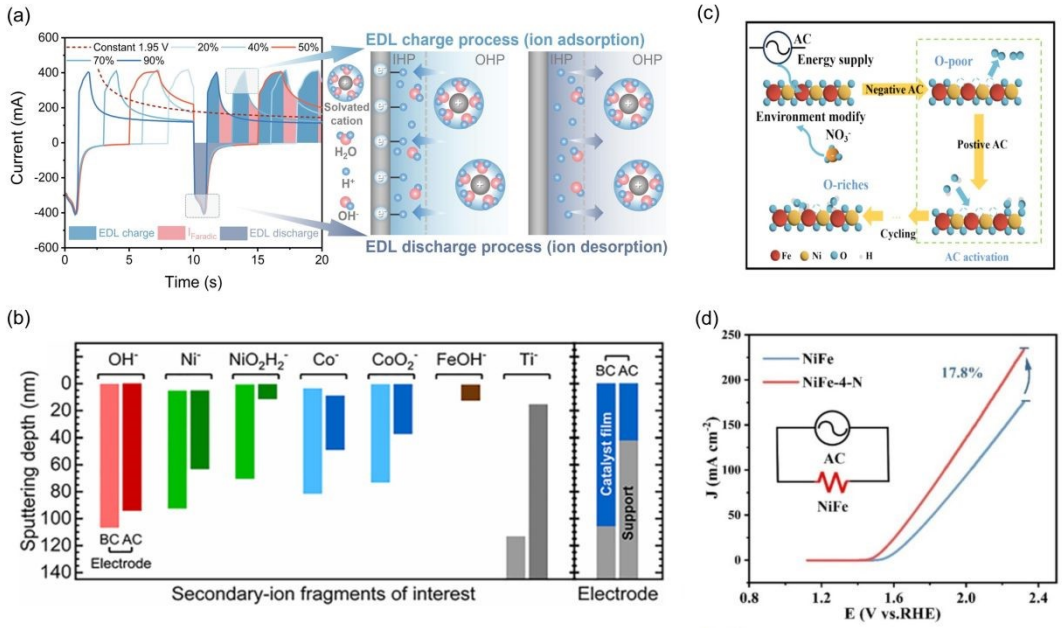

Fig. 19 (a) Effect of pulsed duty cycle on current response and non-Faradaic ion adsorption/desorption in PEMWE. Reproduced with permission.[129] Copyright 2026. Springer. (b)ToF-SIMS depth distribution ranges of various secondary ion fragments before (BC) and after (AC) variable operation tests for $NiCo(OH)_2$/TF. Reproduced with permission.[86] Copyright 2025,Royal Society of Chemistry. (c) Diagram of the functions of AC and nitrate ions in determining the surface structure. (d) LSV curves of NiFe and NiFe-4-N. Reproduced with permission.[130] Copyright 2025, Elsevier.

Meanwhile, sudden shutdowns or power drops in industrial electrolyzer stacks can induce reverse current (RC) phenomena. Due to inconsistent potential decay rates among individual cells, some electrodes may enter reverse-bias states, leading to rapid catalyst-layer degradation.[131] Mullins et al. demonstrated that repeated start-stop cycling caused continuous overpotential growth and irreversible catalyst-layer loss, as confirmed by ToF-SIMS analysis in Fig. 19b.[86] To address this issue, AC pretreatment was proposed to induce controlled catalyst-surface reconstruction, forming a more stable protective layer (Fig. 19c). As shown in Fig. 19d, AC activation enhances current density. During simulated start-stop cycling, the catalyst undergoes alternating high and low potentials but remains structurally intact, confirming the stability of the AC-induced reconstructed layer.[130]

View Article Online
DOI: 10.1039/D6SC03869G

Overall, strategies such as controlled OCP, pulsed operation, and reverse-current protection provide promising approaches for enhancing the long-term stability of renewable-energy-coupled electrolysis systems.

3.3.3 Strategies to Improve the Stability of Device Components

The industrial implementation of the oxygen evolution reaction (OER) faces a critical transition from catalyst-centered intrinsic stability toward system-level durability. Despite substantial advances in the atomic-scale design of electrocatalysts, failures under practical membrane electrode assembly (MEA) operating conditions often originate not from the catalyst itself but from key device components, including bipolar plates (BPs), gas diffusion layers (GDLs), and membranes in Fig. 20a.[132] Corrosion, interfacial delamination, and mass transport limitations in these components typically precede catalyst degradation, rendering them the critical bottlenecks underlying system failure.

BPs are integral components of electrolyzer stacks. Their flow-field channels are responsible for uniformly delivering reactant water to the membrane-electrode interface and efficiently removing gaseous products. BPs must operate stably under harsh conditions involving high pressure as well as strongly oxidative (anode) and reductive (cathode) environments, which impose stringent requirements on electrical conductivity, corrosion resistance, gas impermeability, mechanical strength, and cost effectiveness. Common BP substrates include titanium and stainless steel, as illustrated in Fig. 20b; in contrast to PEM fuel cells, graphite is generally limited to cathodic environments in PEM water electrolysis. For titanium and stainless steel BPs, surface coatings are typically required to maintain low interfacial contact resistance with adjacent components, while coatings on stainless steel must additionally provide robust corrosion protection. Wakayama et al. proposed a cost-effective alternative by sputter-coating titanium BPs with conductive Ti_4O_7, replacing noble-metal coatings such as Au or Pt and effectively suppressing corrosion under high current densities.[133] Similarly, Lettenmeier et al. developed bifunctional Nb/Ti coatings on stainless steel BPs using magnetron sputtering and vacuum plasma spraying, simultaneously enhancing conductivity and corrosion resistance.[134] Beyond materials selection, BP flow-field design critically influences heat dissipation and mass transport in PEMWE systems. An optimal flow field should ensure uniform water distribution and prevent hotspot formation while minimizing pressure drops between channels to reduce pumping losses. In recent years, multiphysics modeling approaches that map the distributions of oxygen

View Article Online
DOI: 10.1039/D6SC03869G

concentration, pressure, temperature, current density, and fluid velocity have emerged as effective tools for optimizing flow-field performance Fig. 20c.[135]

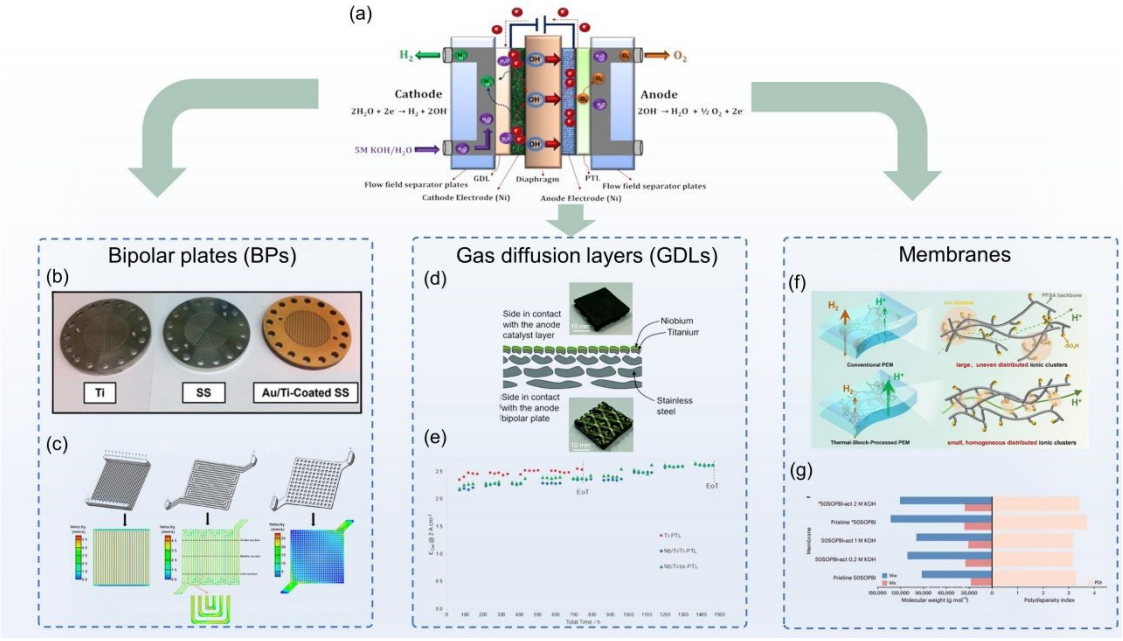

Fig. 20 (a)Schematic of thin titanium GDL functions. Reproduced with permission.[132] Copyright 2022, Elsevier. (b) Examples of bipolar plates made of titanium, stainless steel, and stainless steel coated with a Au/Ti mix. (c) Examples of different flow field architectures and their resulting velocity profiles: parallel flow field, serpentine flow field, and point flow field. Reproduced with permission.[135] Copyright 2025, American Chemical Society. (d) Scheme of the ss-mesh PTL with a plasma-sprayed Nb/Ti coating at the interface with the anode catalyst layer. (e) Accelerated stress test (AST) of cells with the Ti-PTL, Nb/Ti/Ti-PTL and Nb/Ti/ss-PTL. Reproduced with permission.[136] Copyright 2022, Royal Society of Chemistry. (f) Schematic illustration of two membrane structures for PEMWE: conventional PEMs with non-uniform PFSA ionomer distribution, and thermal shock processed PEMs with small and homogeneous distribution. Reproduced with permission.[137] Copyright 2025, Royal Society of Chemistry. (g) Number average molecular weight (Mn), weight-average molecular weight (Mw) and polydispersity index (PDI) of pristine and aged membranes. Reproduced with permission.[138] Copyright 2025, Springer Nature.

Beyond bipolar plates, the stability of the GDLs is equally critical. While maintaining high gas permeability and good electrical conductivity, the GDLs must withstand prolonged redox reactions as well as harsh operating conditions involving elevated temperature and pressure. Any physical damage or pore blockage within the GDL can severely impede gas transport, ultimately leading to a pronounced degradation of overall electrolyzer performance. An ideal GDL therefore requires an optimized porous architecture, appropriate wettability, mechanical robustness, good electrical conductivity, and excellent long-term durability.[139] At present, GDLs are mainly fabricated from carbon-based materials such as carbon paper and carbon cloth, or metallic materials, or metallic materials, including titanium and stainless steel. However, owing to the high anodic oxidation potentials and limited mechanical

strength of carbon materials, they are generally unsuitable for long-term operation under PEMWE conditions. In contrast, metallic GDLs exhibit higher electrical conductivity, superior corrosion resistance, and greater flexibility in constructing diverse porous structures. Accordingly, titanium meshes, felts, foams, and sintered powders have been widely employed as GDLs at the PEMWE anode. Using diffusion bonding techniques, researchers have further fabricated titanium porous sintered layers on titanium meshes.[140] This architecture eliminates the need for dedicated flow fields in the bipolar plates and enables hydrogen output pressures as high as 90 bar, demonstrating considerable potential for commercial applications.[141] In addition, Gago et al. systematically compared coated and uncoated titanium and stainless-steel GDLs (Fig. 20d), revealing that coated GDLs deliver significantly enhanced performance in PEMWE systems. After accelerated stress testing exceeding 1000 h, Nb/Ti metallic coatings were shown to effectively protect stainless-steel GDLs from corrosion (Fig. 20e).[136]

As the core component responsible for proton conduction and gas separation, ionomer membranes are likewise confronted with the dual challenges of chemical degradation and mechanical stress. Widely used perfluorosulfonic acid (PFSA) membranes offer high proton conductivity; however, their carbon-fluorine backbones and ether-containing side chains are susceptible to attack by reactive species generated during electrochemical operation, leading to chain scission and performance decay. To address these issues, strategies have been proposed to enhance backbone crystallinity for increased structural rigidity or to extend side chains and tailor the positioning of sulfonic acid groups. Wang et al. demonstrated that rapid and uniform thermal treatment of a 50 μm-thick PFSA proton exchange membrane selectively activates the rearrangement of sulfonic-acid-rich domains while suppressing excessive crystallization of the C-F backbone, ultimately yielding smaller and more uniformly distributed ionic clusters (Fig. 20f).[137] In parallel, for applications under alkaline conditions, increasing attention has been directed toward non-fluorinated membrane materials. Henkensmeier et al. developed a non-crosslinked sulfonated polybenzimidazole (SOPBI) membrane, in which the introduction of sulfonic acid groups not only enhances hydrophilicity and KOH uptake, but also enables negatively charged imidazole moieties to resist OH^- attack at the C_2 position, thereby improving alkaline stability at the molecular level (Fig. 20g).[138]

Overall, the industrial deployment of the OER urgently requires overcoming durability bottlenecks at the device level. The introduction of corrosion-resistant coatings and optimized flow-field architectures for bipolar plates, the transition of gas diffusion layers from carbon-based to metallic porous materials, and the molecular-level engineering of ionomer membranes to enhance tolerance toward reactive species collectively define the central pathway toward high-efficiency, long-lifetime water electrolysis systems.

4 Conclusions and Outlook

The industrialization of OER electrocatalysts resembles a "Long March of durability." Our understanding of their deactivation mechanisms must therefore evolve from static descriptions to dynamic interpretations. To this end, a multi-scale micro-meso-macro framework has been established to elucidate the origins of electrocatalyst and device degradation failures, including catalyst dissolution and phase changes, lattice-oxygen mechanisms, electrocatalyst leaching, mechanical detachment, and operational, mechanical, and chemical degradation of devices. Based on the aforementioned causes of failure, strategies for enhancing stability are summarized. Despite recent progress in improving electrocatalyst stability and device durability, several challenges persist, and several perspectives of stability could be considered as follows (Fig. 21).

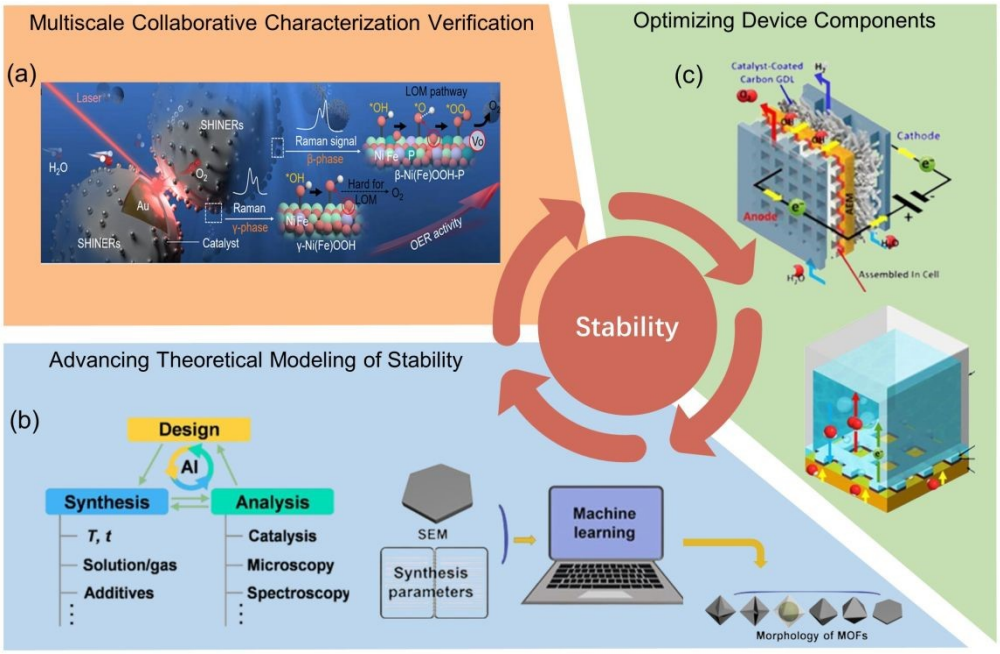

View Article Online
DOI: 10.1039/D6SC03869G

Fig. 21 Outlook on OER stability from the electrocatalyst level to device components. (a) Reproduced with permission.[142] Copyright 2024, American Chemical Society. (b) Reproduced with permission.[143] Copyright 2025, Elsevier. (c) Reproduced with permission.[144] Copyright 2023,Royal Society of Chemistry.

First, Multiscale Collaborative Characterization Verification. Despite significant advances in situ and operando characterization, understanding active-phase evolution and degradation during OER remains incomplete. Most mechanistic insights originate from model half-cell studies that fail to capture the complexity of practical electrolyzers, including high current densities, gas evolution, membrane-electrode interactions, and transport heterogeneities.[145] Consequently, a substantial gap exists between laboratory observations and catalyst behavior under industrial conditions. Bridging this gap requires a shift toward device-relevant operando diagnostics.[146] Future characterization platforms should provide highly penetrative, spatially and temporally resolved measurements of catalyst evolution within realistic membrane-electrode assemblies (MEAs) environments. The integration of synchrotron-based techniques, neutron imaging, and multimodal spectroscopies will enable simultaneous investigation of electronic structure, local reaction environments, gas transport, and degradation processes.[142, 147, 148] Correlative operando methodologies capable of tracking reaction intermediates, active phases, and dissolution products across multiple scales will be essential for elucidating the relationships among catalytic activity, structural reconstruction, lattice oxygen participation, and material loss. Greater attention should also be given to transient and non-equilibrium operating conditions, where degradation is often accelerated.

Second, Advancing Theoretical Modeling of Stability. The assessment and prediction of OER electrocatalyst stability require a shift from empirical characterization to quantitative, theory- and data-driven frameworks.[149, 150] Static DFT calculations cannot capture dynamic adsorption or local pH gradients at operating interfaces. Future studies should employ constant-potential AIMD with explicit solvent double layers to realistically model electrochemical environments. To overcome the spatial and temporal limitations of DFT, universal machine-learning interatomic potentials can enable larger-scale, nanosecond-timescale simulations. For multicomponent oxides undergoing surface reconstruction, active-learning workflows combined with simulated annealing are essential to explore potential energy surfaces and identify undercoordinated active sites. A standardized set of stability descriptors, such as metal dissolution energy, oxygen-vacancy formation energy, surface reconstruction tendency, Pourbaix stability, corrosion resistance, current retention, and

View Article Online
DOI: 10.1039/D6SC03869G

activity decay constant, should be integrated into high-throughput computational databases and correlated with experimental metrics under unified testing protocols. Machine-learning models built on this descriptor-database framework can screen stable catalysts, predict degradation kinetics under different conditions, and identify dominant failure mechanisms.[143, 151, 152] Such approaches improve reproducibility, comparability, and predictive power, guiding rational design of durable, high-performance OER electrocatalysts.

Third, Optimizing Device Components. As the core reactor of water electrolysis, the electrolyzer architecture largely determines whether the intrinsic activity of electrocatalysts can be translated into practical performance. Although water splitting is chemically simple, it involves coupled processes across multiple length scales, including interfacial charge transfer, reactant and ion transport, and the nucleation, growth, and removal of gas bubbles.[153] Consequently, water electrolysis is inherently a multiscale and multiphysics process in which reaction kinetics and transport phenomena are tightly coupled. Efficient electrolyzers should minimize ohmic and hydraulic losses while facilitating rapid transport of reactants and products, thereby maximizing catalyst utilization.[144, 154] Therefore, improving catalyst activity alone is insufficient. Highly active and durable catalytic sites must be uniformly integrated over large electrode areas, while the electrolyzer structure should be engineered to ensure efficient mass, momentum, and heat transfer throughout the device. Unlike conventional chemical reactors, electrolyzers also involve electric fields that strongly influence transport behavior and reaction environments. As a result, the design of next-generation electrolyzers requires moving beyond the traditional framework of transport phenomena and reaction engineering toward a deeper understanding of electrochemically coupled transport processes. This calls for multiscale models and multiphysics simulations that integrate mass, momentum, heat, and charge transport, providing a scientific basis for the rational design of high-performance electrolyzers.

In summary, dynamic reconstruction is central to OER catalysis, enabling activity enhancement while driving structural degradation. Integrating operando characterization, dynamic modeling, multiphysics simulation, and device engineering can translate reconstruction chemistry into practical design principles, enabling active control of catalyst evolution and durable OER catalysts for industrial green hydrogen production.

View Article Online
DOI: 10.1039/D6SC03869G

Data availability

No primary research results, software, or code have been included, and no new data were generated or analyzed as part of this review.

Author contributions

Xia Chen contributed to writing the original draft, investigation, and literature collection. Chengming Huang, Jin Liu and Qiong Xiang collected papers related to the topic. Ling Zhang provided academic guidance during the preparation of the manuscript. Xun Huang contributed to the development of the review framework. Li Li conceived the review topic, designed the overall framework and scientific scope of the review. Zidong Wei provided resources. The manuscript was revised by all authors.

Conflicts of interest

The authors declare no competing financial interest.

Acknowledgments

This work was supported by the National Key Research and Development Program of China (2021YFB4000300) and the National Natural Science Foundation of China (21822803 and U24A20541).

References

1. Q. L. Ma and S. C. Mu, *Interdiscip. Mater.*, 2023, **2**, 53-90.
2. Y. T. Wang, Y. D. Xue and A. Züttel, *Chem. Soc. Rev.*, 2024, **53**, 972-1003.
3. L. Ren, Y. H. Li, N. Zhang, Z. Li, X. Lin, W. Zhu, C. Lu, W. J. Ding and J. X. Zou, *Nano-Micro Lett.*, 2023, **15**, 93.
4. A. Odenweller and F. Ueckerdt, *Nat. Energy*, 2025, **10**, 110-123.
5. F. Ueckerdt, P. C. Verpoort, R. Anantharaman, C. Bauer, F. Beck, T. Longden and S. Roussanaly, *Joule*, 2024, **8**, 104-128.
6. S. A. Dristy, M. A. Habib, S. Lin, M. H. Joni, R. Mandavkar, Y. U. Chung, M. Najibullah and J. Lee, *Acta Physico-Chimica Sinica*, 2025, **41**, 100079.

View Article Online
DOI: 10.1039/D6SC03869G

7. Q. Y. Hu, L. Zhang and H. M. Chen, *Chemcatchem*, 2025, **17**, e00170.
8. L. Zhang, W. Y. Wu, Q. Y. Hu, S. D. Yang, L. Li, R. J. Liao and Z. D. Wei, *J. Electrochem.*, 2025, **31**, 2515007.
9. Y. W. Su, H. Wu, S. Y. Wang, Z. Hu, J. Li, J. W. Chang, G. C. Yin and S. Y. Lu, *J. Energy Chem.*, 2025, **106**, 331-339.
10. X. Chen, X. Q. Zheng, C. M. Huang, S. Y. Lv, Q. Xiang, J. Liu, L. Li and Z. D. Wei, *J. Mater. Chem. A*, 2025, **13**, 33188-33195.
11. Q. Dang, H. Lin, Z. Fan, L. Ma, Q. Shao, Y. Ji, F. Zheng, S. Geng, S. Z. Yang, N. Kong, W. Zhu, Y. Li, F. Liao, X. Huang and M. Shao, *Nat. Commun.*, 2021, **12**, 6007.
12. J. Y. Tang, D. Q. Guan, H. Y. Xu, L. Q. Zhao, U. Arshad, Z. J. Fang, T. J. Zhu, M. Kim, C. W. Pao, Z. W. Hu, J. J. Ge and Z. P. Shao, *Nat. Commun.*, 2025, **16**, 801.
13. Z. Chen, B. H. Hu, X. Y. Zhang, K. Zong, L. Yang, Y. Wang, X. Wang, S. Q. Song and Z. W. Chen, *Electrochem. Energy Rev.*, 2025, **8**.
14. R. D. Wan, T. H. Yuan, L. C. Wang, B. Li, M. L. Liu and B. T. Zhao, *Nat. Catal.*, 2024, **7**, 1288-1304.
15. J. Ni, Z. P. Shi, Y. B. Wang, J. H. Yang, H. X. Wu, P. B. Wang, M. L. Xiao, C. P. Liu and W. Xing, *eScience*, 2025, **5**, 100295.
16. H. J. W. Li, Y. Lin, J. Y. Duan, Q. L. Wen, Y. W. Liu and T. Y. Zhai, *Chem. Soc. Rev.*, 2024, **53**, 10709-10740.
17. X. Wu, Z. Shao, Q. Zhu, X. Hou, C. Wang, J. Zeng, K. Huang and S. Feng, *ACS Catal.*, 2024, **14**, 5888-5897.
18. Z. Li, Y. E. Zhou, M. H. Xie, H. Cheng, T. Wang, J. Chen, Y. Lu, Z. L. Tian, Y. Q. Lai and G. H. Yu, *Angew. Chem. Int. Ed.*, 2023, **62**.
19. H. B. Tao, H. Liu, K. J. Lao, Y. P. Pan, Y. B. Tao, L. R. Wen and N. F. Zheng, *Nat. Nanotechnol.*, 2024, **19**, 1074-1076.
20. L. Tao, F. Lv, D. W. Wang, H. Luo, F. X. Lin, H. Y. Gong, H. T. Mi, S. G. Wang, Q. H. Zhang, L. Gu, M. C. Luo and S. J. Guo, *Joule*, 2024, **8**, 450-460.
21. M. Geuss, L. Löttert, T. Böhm, A. Hutzler, K. J. J. Mayrhofer, S. Thiele and S. Cherevko, *ACS Catal.*, 2024, **14**, 11819-11831.
22. C. Qiao, Q. Wu, L. Hao, Y. Z. Wang, X. Sun, Q. C. Zou and X. Z. An, *Corros. Sci.*, 2023, **221**, 111359.
23. C. Qiu, Z. K. Xu, F. Y. Chen and H. T. Wang, *ACS Catal.*, 2024, **14**, 921-954.

24. L. J. Li, P. C. M. Laan, X. Y. Yan, X. J. Cao, M. J. Mekkering, K. Zhao, L. Ke, X. Y. Jiang, X. Y. Wu, L. J. Li, L. J. Xue, Z. P. Wang, G. Rothenberg and N. Yan, *Adv. Sci.*, 2023, **10**, 2206180.
25. X. B. Zheng, J. R. Yang, X. Xu, S. X. Dou, W. P. Sun, D. S. Wang and G. X. Wang, *Adv. Energy Mater.*, 2024, **14**, 2401227.
26. Y. B. Chen, D. J. Zheng, Z. J. Xu and Y. Shao-Horn, *Nat. Sustain.*, 2024, **7**, 371-374.
27. Y. T. Sun, Y. H. Li, L. M. Dai, N. L. D. Sui, W. J. Fan, Y. T. Zhou, J. W. Zhu and J. M. Lee, *Adv. Funct. Mater.*, 2025, **35**, 2419626.
28. R. Yanagi, P. Yang, A. W. Tricker, Y. Chen, M. C. Scott, S. A. Berlinger, I. V. Zenyuk and X. Peng, *Joule*, 2025, **9**, 102001.
29. X. X. Li, C. Tang, L. C. Cong, K. J. Wu, J. H. Liu, J. C. Dong, S. Chen and Q. Zhang, *Angew. Chem. Int. Ed.*, 2025, **64**, e202510448.
30. W. J. He, Y. S. Wang, Y. L. Zhao, C. Tang, L. C. Cong, C. L. Wang, Y. Lu, X. Liu, J. C. Dong, S. Cherevko, Q. S. Hua and Q. Zhang, *J. Am. Chem. Soc.*, 2025.
31. C. M. Huang, W. J. Zhang, J. Li and Z. D. Wei, *J. Phys. Chem. C*, 2023, **127**, 12827-12840.
32. R. A. Marquez, M. Espinosa, E. Kalokowski, Y. J. Son, K. Kawashima, T. V. Le, C. E. Chukwuneke and C. B. Mullins, *ACS Energy Lett.*, 2024, **9**, 547-555.
33. S. Z. Oener, A. Bergmann and B. R. Cuenya, *Nat. Synth.*, 2023, **2**, 817-827.
34. R. Martínez-Hincapié, J. Timoshenko, T. Wagner, E. Ortega, J. Druce, M. C. O. Monteiro, M. Rüscher, J. Jang, E. Alagöz, S. Lasagna, L. Jacobse, A. Bergmann, B. R. Cuenya and S. Z. Oener, *Nat. Chem.*, 2025, 1-9.
35. M. H. Ning, S. N. Wang, J. Wan, Z. C. Xi, Q. Chen, Y. M. Sun, H. Li, T. Y. Ma and H. Y. Jin, *Angew. Chem. Int. Ed.*, 2024, **63**, e202415794.
36. H. Zhang, L. Chen, F. Dong, Z. W. Lu, E. M. Lv, X. L. Dong, H. X. Li, Z. Y. Yuan, X. W. Peng, S. H. Yang, J. S. Qiu, Z. X. Guo and Z. H. Wen, *Energy Environ. Sci.*, 2024, **17**, 6435-6481.
37. M. Milosevic, T. Böhm, A. Körner, M. Bierling, L. Winkelmann, K. Ehelebe, A. Hutzler, M. Suermann, S. Thiele and S. Cherevko, *ACS Energy Lett.*, 2023, **8**, 2682-2688.
38. H. H. Heenen, H. S. Pillai, K. Reuter and V. J. Bukas, *Nat. Catal.*, 2025, **8**, 853-854.
39. Y. Hu, H. W. Chen and Q. Y. Lu, *J. Phys. Chem. C*, 2022, **126**, 18198−18207.

40. C. Han, Y. Lv, X. Tang, S. X. Zhang, Y. J. Jiang, Z. Y. Lu and S. Dai, *Nano Lett.*, 2025, **25**, 11484-11491.
41. K. Du, L. F. Zhang, J. Q. Shan, J. X. Guo, J. Mao, C. C. Yang, C. H. Wang, Z. P. Hu and T. Ling, *Nat. Commun.*, 2022, **13**, 5448.
42. C. Y. Hao, X. N. Li, H. L. Huang, L. B. Ge, Z. P. Fu, Y. L. Lu, Y. Wang, S. J. Zhang and Z. X. Cheng, *ACS Energy Lett.*, 2023, **8**, 4506-4513.
43. B. Elkamash and F. Hess, *J. Mater. Chem. A*, 2025, **13**, 12566-12580.
44. X. W. Tao, L. Hou, X. Y. Wang, J. Jin, H. A. Li and F. M. Gao, *Nat. Commun.*, 2025, **16**, 8788.
45. L. S. Peng, N. Yang, Y. Q. Yang, Q. Wang, X. Y. Xie, D. Sun-Waterhouse, L. Shang, T. R. Zhang and G. I. N. Waterhouse, *Angew. Chem. Int. Ed.*, 2021, **60**, 24612-24619.
46. Y. Duan, J. Y. Lee, S. B. Xi, Y. M. Sun, J. J. Ge, S. J. H. Ong, Y. B. Chen, S. Dou, F. X. Meng, C. Z. Diao, A. C. Fisher, X. Wang, G. G. Scherer, A. Grimaud and Z. C. J. Xu, *Angew. Chem. Int. Ed.*, 2021, **60**, 7418-7425.
47. W. J. Li, D. M. Chen, Z. X. Lou, H. Y. Yuan, X. P. Fu, H. Y. Lin, M. Y. Lin, Y. Hou, H. F. Qi, P. F. Liu, H. G. Yang and H. F. Wang, *J. Am. Chem. Soc.*, 2025, **147**, 10446-10458.
48. C. Wei, Z. B. Wang, K. Otani, D. Hochfilzer, K. Zhang, R. Nielsen, I. Chorkendorff and J. Kibsgaard, *ACS Catal.*, 2023, **13**, 14058-14069.
49. S. Geiger, O. Kasian, M. Ledendecker, E. Pizzutilo, A. M. Mingers, W. T. Fu, O. Diaz-Morales, Z. Z. Li, T. Oellers, L. Fruchter, A. Ludwig, K. J. J. Mayrhofer, M. T. M. Koper and S. Cherevko, *Nat. Catal.*, 2018, **1**, 508-515.
50. C. Lin, J. L. Li, X. P. Li, S. Yang, W. Luo, Y. J. Zhang, S. H. Kim, D. H. Kim, S. S. Shinde, Y. F. Li, Z. P. Liu, Z. Jiang and J. H. Lee, *Nat. Catal.*, 2021, **4**, 1012-1023.
51. F. Q. Wang, P. C. Zou, Y. Y. Zhang, W. L. Pan, Y. Li, L. M. Liang, C. Chen, H. Liu and S. J. Zheng, *Nat. Commun.*, 2023, **14**, 6019.
52. Z. Liu, Y. Zi, S. Zhu, Y. Zhang, C. Zhang and J. Hu, *J Colloid Interface Sci*, 2025, **707**, 139698.
53. K. J. May, C. E. Carlton, K. A. Stoerzinger, M. Risch, J. Suntivich, Y. L. Lee, A. Grimaud and Y. Shao-Horn, *J. Phys. Chem. Lett.*, 2012, **3**, 3264-3270.
54. D. Vivona, K. Gordiz, R. Meyer, S. Raman and Y. Shao-Horn, *J. Mater. Chem. A*, 2024, **12**, 22737-22755.

55. T. Priamushko, E. Franz, A. Logar, L. Bijelic, P. Guggenberger, D. Escalera-López, M. Zlatar, J. Libuda, F. Kleitz, N. Hodnik, O. Brummel and S. Cherevko, *J. Am. Chem. Soc.*, 2025, **147**, 3517-3528.

56. C. Jing, L. L. Li, Y. Y. Chin, C. W. Pao, W. H. Huang, M. M. Liu, J. Zhou, T. T. Yuan, X. Q. Zhou, Y. F. Wang, C. T. Chen, D. W. Li, J. Q. Wang, Z. W. Hu and L. J. Zhang, *Acs Nano*, 2024, **18**, 14496-14506.

57. C. L. Rong, S. H. Wang, X. Shen, C. Jia, Q. Sun, Q. Zhang and C. Zhao, *Energy Environ. Sci.*, 2024, **17**, 4196-4204.

58. R. A. Marquez, E. Kalokowski, M. Espinosa, J. T. Bender, Y. J. Son, K. Kawashima, C. E. Chukwuneke, L. A. Smith, H. Celio, A. Dolocan, X. Zhan, N. Miller, D. J. Milliron, J. Resasco and C. B. Mullins, *Energy Environ. Sci.*, 2024, **17**, 2028-2045.

59. Y. Zeng, M. T. Zhao, Z. H. Huang, W. J. Zhu, J. X. Zheng, Q. Jiang, Z. C. Wang and H. F. Liang, *Adv. Energy Mater.*, 2022, **12**, 2201713.

60. H. Y. Zhong, Q. Zhang, J. C. Yu, X. Zhang, C. Wu, Y. F. Ma, H. An, H. Wang, J. Zhang, X. P. Wang and J. M. Xue, *Adv. Energy Mater.*, 2023, **13**, 2301391.

61. F. Y. Chen, Z. Y. Wu, Z. Adler and H. T. Wang, *Joule*, 2021, **5**, 1704-1731.

62. Q. Zhang, H. Y. Zhong, C. Wu, J. C. Yu, Z. G. Yu, C. Z. Diao, X. M. Li, Y. N. Hua, S. B. Xi, X. P. Wang and J. M. Xue, *Acs Nano*, 2025, **19**, 39480-39490.

63. S. Qi, J. You, X. Y. Liufu, Y. Zhang, R. B. Chen, J. P. Zhuang, T. Y. Liang, L. L. Li, Q. H. Huo, C. Y. Shang, X. Zhang, H. P. Yang, Q. Hu and C. X. He, *Adv. Mater.*, 2025, e12188.

64. K. X. Zhang, X. Liang, Y. C. Wang, Y. C. Zou, X. Zhao, H. Chen and X. X. Zou, *Nat. Commun.*, 2025, **16**, 8164.

65. Z. Zhang, X. Y. Ren, W. Y. Dai, H. Zhang, Z. Y. Sun, Z. Ye, Y. Hou, P. Z. Liu, B. S. Xu, L. H. Qian, T. Liao, H. X. Zhang, J. J. Guo and Z. Q. Sun, *Adv. Sci.*, 2024, **11**, 2408754.

66. H. Chen, L. N. Wang, M. H. Na and X. X. Zou, *Chem. Sci.*, 2025, **16**, 20662-20676.

67. N. Deka, T. E. Jones, L. J. Falling, L. E. Sandoval-Diaz, T. Lunkenbein, J. J. Velasco-Velez, T. S. Chan, C. H. Chuang, A. Knop-Gericke and R. V. Mom, *ACS Catal.*, 2023, **13**, 7488-7498.

68. Y. Hu, Y. Zheng, J. Jin, Y. T. Wang, Y. Peng, J. Yin, W. Shen, Y. C. Hou, L. Zhu, L. An, M. Lu, P. X. Xi and C. H. Yan, *Nat. Commun.*, 2023, **14**, 1949.

69. F. Zeng, C. Mebrahtu, L. F. Liao, R. Palkovits and A. K. Beine, *J. Energy Chem.*, 2022, **69**, 301-329.

70. J. Wang, S. J. Kim, J. P. Liu, Y. Gao, S. Choi, J. Han, H. Shin, S. Jo, J. Kim, F. Ciucci, H. Kim, Q. T. Li, W. L. Yang, X. Long, S. H. Yang, S. P. Cho, K. H. Chae, M. G. Kim, H. Kim and J. Lim, *Nat. Catal.*, 2021, **4**, 212-222.

71. J. Z. Huang, Z. Y. Zhang, C. Spezzati, A. H. Clark, N. Hales, N. S. Genz, N. Daffé, R. Skoupy, L. Gubler, I. E. Castelli, T. J. Schmidt and E. Fabbri, *Nat. Commun.*, 2025, **16**, 7518.

72. L. Yu, X. Chen, S. D. Cheng, T. F. Zhong, R. F. Zhou, Z. H. Deng and L. Li, *Nanoscale*, 2025, **17**, 4485-4493.

73. L. Y. Ran, K. Zhao, X. Y. Jiang and N. Yan, *J. Mater. Chem. A*, 2025, **13**, 26804-26811.

74. N. Yang, Z. F. Qi, H. A. Li, X. Lin, W. F. Lin, S. Georgiadou, F. He, L. Hong and Z. H. Wang, *J. Energy Chem.*, 2025, **105**, 669-701.

75. A. Angulo, P. van der Linde, H. Gardeniers, M. Modestino and D. F. Rivas, *Joule*, 2020, **4**, 555-579.

76. J. Kim, S. M. Jung, N. Lee, K. S. Kim, Y. T. Kim and J. K. Kim, *Adv. Mater.*, 2023, **35**, 2305844.

77. T. T. Xu, Q. Liang, F. X. Liu, Z. Z. Zhao, W. W. Li, A. F. Wei, M. Q. Liu, K. X. Song, B. B. Yang, T. W. Dong, X. Zou, W. Zhang and W. T. Zheng, *Adv. Funct. Mater.*, 2025, e22894.

78. V. Sharma, R. Dhiman and A. Mahajan, *Appl. Surf. Sci.*, 2023, **612**, 155883.

79. F. Bizzotto, J. Quinson, J. Schröder, A. Zana and M. Arenz, *J. Catal.*, 2021, **401**, 54-62.

80. W. Z. Zhang, M. H. Liu, X. Gu, Y. X. Shi, Z. F. Deng and N. S. Cai, *Chem. Rev.*, 2023, **123**, 7119-7192.

81. W. Wang, B. Q. Yuan, Q. Sun and R. Wennersten, *J. Energy Storage*, 2022, **52**.

82. S. M. Alia, K. S. Reeves, D. A. Cullen, H. R. Yu, A. J. Kropf, N. Kariuki, J. H. Park and D. J. Myers, *J. Electrochem. Soc.*, 2024, **171**, 044503.

83. Z. Y. Rui, K. Hua, Z. L. Dou, A. D. Tan, C. Y. Zhang, X. Y. Shi, R. Ding, X. K. Li, X. Duan, Y. K. Wu, Y. P. Zhang, X. B. Wang, J. Li and J. G. Liu, *J. Mater. Chem. A*, 2024, **12**, 9563-9573.

84. T. Srour, K. Kumar, V. Martin, L. Dubau, F. Maillard, B. Gilles, J. Dillet, S. Didierjean, B. Amoury, T. D. Le and G. Maranzana, *Int. J. Hydrogen Energy*, 2024, **58**, 351-361.

85. M. A. Riaz, P. Trogadas, D. Ayme-Perrot, C. Sachs, N. Dubouis, H. Girault and M. O. Coppens, *Energy Environ. Sci.*, 2025, **18**, 5190-5214.

86. R. A. Marquez, J. T. Bender, A. M. Aleman, E. Kalokowski, T. V. Le, C. L. Williamson, M. L. Frederiksen, K. Kawashima, C. E. Chukwuneke, A. Dolocan, D. J. Milliron, J. Resasco, T. F. Jaramillo and C. B. Mullins, *Energy Environ. Sci.*, 2025, **18**, 7170-7187.

87. X. Liu, R. T. Guo, K. Ni, F. J. Xia, C. J. Niu, B. Wen, J. S. Meng, P. J. Wu, J. S. Wu, X. J. Wu and L. Q. Mai, *Adv. Mater.*, 2020, **32**, 2001136.

88. Y. D. Yao, G. M. Zhao, X. Y. Guo, P. Xiong, Z. H. Xu, L. H. Zhang, C. S. Chen, C. Xu, T. S. Wu, Y. L. Soo, Z. M. Cui, M. M. J. Li and Y. Zhu, *J. Am. Chem. Soc.*, 2024, **146**, 15219-15229.

89. Y. Wang, Y. Z. Zhao, L. Liu, W. J. Qin, S. J. Liu, J. P. Tu, Y. D. Liu, Y. P. Qin, J. F. Liu, H. Y. Wu, D. Y. Zhang, A. M. Chu, B. R. Jia, X. H. Qu, M. L. Qin and J. M. Xue, *J. Am. Chem. Soc.*, 2023, **145**, 20261-20272.

90. D. R. Yang, C. Y. Zhang, Y. F. Qin, Y. Yue, Y. B. Liu, X. Y. Shi, K. Hua, X. M. An, L. Y. Jin, Y. P. Zhang, S. W. Zuo, A. D. Tan and J. G. Liu, *Nat. Commun.*, 2025, **16**, 7236.

91. Z. H. Xiao, Y. C. Huang, C. L. Dong, C. Xie, Z. J. Liu, S. Q. Du, W. Chen, D. F. Yan, L. Tao, Z. W. Shu, G. H. Zhang, H. G. Duan, Y. Y. Wang, Y. Q. Zou, R. Chen and S. Y. Wang, *J. Am. Chem. Soc.*, 2020, **142**, 12087-12095.

92. Y. J. Wu, J. Yang, T. X. Tu, W. Q. Li, P. F. Zhang, Y. Zhou, J. F. Li, J. T. Li and S. G. Sun, *Angew. Chem. Int. Ed.*, 2021, **60**, 26829-26836.

93. Y. X. Li, Z. Zhang, C. G. Li, X. Y. Hou, J. R. Zeng, X. B. Chen, Z. Shi and S. H. Feng, *Adv. Funct. Mater.*, 2025, **35**, 2417983.

94. F. Zhang, K. Wang, H. Zhang, S. L. Yang, M. Xu, Y. He, L. C. Lei, P. F. Xie and X. W. Zhang, *Adv. Funct. Mater.*, 2025, **35**, 2500861.

95. J. H. Zhang, X. B. Fu, S. Kwon, K. F. Chen, X. Z. Liu, J. Yang, H. R. Sun, Y. C. Wang, T. Uchiyama, Y. Uchimoto, S. F. Li, Y. Li, X. L. Fan, G. Chen, F. J. Xia, J. S. Wu, Y. B. Li, Q. Yue, L. Qiao, D. Su, H. Zhou, W. A. Goddard and Y. J. Kang, *Science*, 2025, **387**, 48-55.

96. Y. D. Liu, R. X. Deng, Y. Song, W. L. Tan, X. X. Tao, S. J. Luo, D. J. Long, S. G. Chen and Z. D. Wei, *Chem. Commun.*, 2025, **61**, 4547-4550.

97. L. S. Peng, J. Wang, Y. Nie, K. Xiong, Y. Wang, L. Zhang, K. Chen, W. Ding, L. Li and Z. D. Wei, *ACS Catal.*, 2017, **7**, 8184-8191.

98. W. B. Wang, Q. L. Wen, D. J. Huang, Y. Lin, N. D. Zhao, L. Tang, M. Li, Y. W. Liu and R. X. He, *Angew. Chem. Int. Ed.*, 2025, **64**, e202415132.

99. Y. Qin, T. T. Yu, S. H. Deng, X. Y. Zhou, D. M. Lin, Q. Zhang, Z. Y. Jin, D. F. Zhang, Y. B. He, H. J. Qiu, L. H. He, F. Y. Kang, K. K. Li and T. Y. Zhang, *Nat. Commun.*, 2022, **13**, 3784.

100. X. Y. Ping, Y. D. Liu, L. X. Zheng, Y. Song, L. Guo, S. G. Chen and Z. D. Wei, *Nat. Commun.*, 2024, **15**, 2501.

101. Q. Wu, Q. P. Gao, X. P. Wang, Y. P. Qi, L. Shen, X. S. Tai, F. Yang, X. He, Y. Wang, Y. C. Yao, Y. C. Ren, Y. L. Luo, S. J. Sun, D. D. Zheng, Q. Liu, S. Alfaifi, X. P. Sun and B. Tang, *iScience*, 2024, **27**, 108738.

102. J. Kwon, S. Sun, S. Choi, K. Lee, S. Jo, K. Park, Y. K. Kim, H. B. Park, H. Y. Park, J. H. Jang, H. Han, U. Paik and T. Song, *Adv. Mater.*, 2023, **35**, 2300091.

103. Y. Wang, R. Yang, Y. Ding, B. Zhang, H. Li, B. Bai, M. Li, Y. Cui, J. Xiao and Z. S. Wu, *Nat. Commun.*, 2023, **14**, 1412.

104. S. L. Li, Z. X. Zhou, J. H. Li, Y. Xiao, Y. Yuan, H. Zhu, F. C. Cui, X. F. Jing and G. S. Zhu, *Chem. Sci.*, 2025, **16**, 12568-12576.

105. H. Li, J. S. Xia, J. J. Zheng, X. Bai, Q. L. Ren, W. J. Hao, Q. Y. Bi, G. S. Li and J. C. Fan, *Adv. Funct. Mater.*, 2025, e25383.

106. K. Du, L. F. Zhang, J. Q. Shan, J. X. Guo, J. Mao, C. C. Yang, C. H. Wang, Z. P. Hu and T. Ling, *Nat. Commun.*, 2022, **13**, 5448.

107. Q. Wu, Q. P. Gao, L. M. Sun, H. M. Guo, X. S. Tai, D. Li, L. Liu, C. Y. Ling and X. P. Sun, *Chin. J. Catal.*, 2021, **42**, 482-489.

108. S. G. Sun, Z. Q. Wan, Y. Y. Xu, X. M. Zhou, W. Gao, J. J. Qian, J. Gao, D. Cai, Y. J. Ge, H. G. Nie and Z. Yang, *Acs Nano*, 2025, **19**, 12090-12101.

109. J. Y. Li, X. H. Yu, W. Huang, Q. Zhang, K. Wei, X. Y. Zhou, Y. M. Zhu, X. P. Zhong, M. Yeh, N. Alonso-Vante and J. W. Ma, *Angew. Chem. Int. Ed.*, 2025, **64**, e202511750.

110. Y. Liu, Y. Huang, D. J. Wu, H. Jang, J. H. Wu, H. R. Li, W. X. Li, F. Zhu, M. G. Kim, D. L. Zhou, X. K. Xi, Z. W. Lei, Y. C. Zhang, Y. Deng, W. S. Yan, M.

D. Gu, J. Jiang, S. H. Jiao and R. G. Cao, *J. Am. Chem. Soc.*, 2024, **146**, 26897-26908.

111. X. Ren, C. Wei, Y. M. Sun, X. Z. Liu, F. Q. Meng, X. X. Meng, S. N. Sun, S. B. Xi, Y. H. Du, Z. F. Bi, G. Y. Shang, A. C. Fisher, L. Gu and Z. C. J. Xu, *Adv. Mater.*, 2020, **32**, 2001292.
112. C. Lin, T. Y. Chen, T. Zhou, Y. Q. Wu, C. K. T. Wun, W. C. Chen, H. Y. Chen, V. C. Tung, Z. X. Guo, T. W. B. Lo, L. Cai, Y. D. Deng and P. C. Y. Chow, *ACS Energy Lett.*, 2025, **10**, 2641-2649.
113. Y. C. Pi, Y. Xu, L. G. Li, T. Sun, B. L. Huang, L. Z. Bu, Y. H. Ma, Z. W. Hu, C. W. Pao and X. Q. Huang, *Adv. Funct. Mater.*, 2020, **30**, 2004375.
114. J. Y. Li, Y. M. Zhu, C. Y. Li, Q. Zhang, J. Rong, S. S. Guo, N. Alonso-Vante, L. Yang, M. H. Yeh, W. H. Huang, X. H. Yu, H. F. Cheng and J. W. Ma, *Nat. Commun.*, 2025, **16**, 8827.
115. A. Li, X. X. Tang, R. J. Cao, D. C. Song, F. Z. Wang, H. Yan, H. M. Chen and Z. D. Wei, *Adv. Mater.*, 2024, **36**, 2401818.
116. C. Huang, C. A. Triana, B. Q. Jia, N. Dongfang, R. Erni, D. F. Abbott, R. N. Durr, H. Zhao, V. Mougel, M. Iannuzzi and G. R. Patzke, *Acs Nano*, 2025, **19**, 41888-41899.
117. J. Y. Fan, J. D. Jiang, Y. Y. Wang, X. S. Zhang, Y. Liu, X. Yang, T. Pan, D. D. Xu, N. E. Shi, Y. Lin, M. Han and H. Pang, *Adv. Funct. Mater.*, 2025, **35**, 2425770.
118. Q. Zhang, W. Xiao, H. C. Fu, X. L. Li, J. L. Lei, H. Q. Luo and N. B. Li, *ACS Catal.*, 2023, **13**, 14975-14986.
119. R. Y. Fan, J. Y. Xie, H. J. Liu, H. Y. Wang, M. X. Li, N. Yu, R. N. Luan, Y. M. Chai and B. Dong, *Chem. Eng. J*, 2022, **431**, 134040.
120. Q. L. Wen, T. Y. Liu, D. J. Huang, Y. Lin, Z. H. Yang, R. O. Yang, Y. W. Liu, X. M. Ai, J. K. Fang, Y. F. Li, B. Y. Xia, S. J. Cheng and T. Y. Zhai, *Angew. Chem. Int. Ed.*, 2025, **64**, e202509915.
121. W. J. Shi, T. H. Shen, C. K. Xing, K. Sun, Q. S. Yan, W. Z. Niu, X. Yang, J. J. Li, C. Y. Wei, R. J. Wang, S. Q. Fu, Y. Yang, L. Y. Xue, J. F. Chen, S. W. Cui, X. Y. Hu, K. Xie, X. Xu, S. Duan, Y. F. Xu and B. Zhang, *Science*, 2025, **387**, 791-796.
122. C. J. Chen, Y. Zheng and S. Z. Qiao, *Natl. Sci. Rev.*, 2024, **11**, nwae250.

123. H. Y. Zeng, Z. F. Liu, J. Qi, J. J. Chen, Y. Q. Zeng, C. Y. Yang, Z. Z. Li, C. Wang, L. Gu, Y. Zhang, M. Shu and C. Z. Yang, *Energy Environ. Mater.*, 2025, **8**, e12813.

124. L. Wang, Y. Hao, J. Pan, S. Bi, S.-F. Hung, K.-S. Peng, A.-Y. Wang, T.-Y. Chen, S. Li, C. Ling, Y. Zhang, L. Li, F. Hu, X. Zhou, H.-Y. Chen, K. Wu, J. Wang, Y. Wu and S. Peng, *Nat. Catal.*, 2026, 1-11.

125. J. Liang, J. Li, H. L. Dong, Z. X. Z. Li, X. He, Y. Wang, Y. c. Yao, Y. C. Ren, S. j. Sun, Y. S. Luo, D. D. Zheng, J. Li, Q. Liu, F. M. Luo, T. W. Wu, G. Chen, X. P. Sun and B. Tang, *Nat. Commun.*, 2024, **15**, 6208.

126. J. Z. Huang, A. H. Clark, N. Hales, K. Crossley, J. Guehl, R. Skoupy, T. J. Schmidt and E. Fabbri, *Nat. Chem.*, 2025, **17**.

127. M. Görlin, J. H. Stenlid, S. Koroidov, H. Y. Wang, M. Börner, M. Shipilin, A. Kalinko, V. Murzin, O. V. Safonova, M. Nachtegaal, A. Uheida, J. Dutta, M. Bauer, A. Nilsson and O. Diaz-Morales, *Nat. Commun.*, 2020, **11**, 6181.

128. E. R. Sauve, B. Y. Tang, N. K. Razdan, W. L. Toh, S. Weng and Y. Surendranath, *Joule*, 2024, **8**, 728-745.

129. X. Zhang, W. Zhou, X. Meng, Y. Huang, Y. Yu, H. Zhao, L. Wang, F. Sun, J. Gao and G. Zhao, *Nano-Micro Lett.*, 2026, **18**, 103.

130. C. Y. Cai, Z. L. Zhang, Y. T. Hua, Z. H. Zhang, Y. T. Wu, K. Wang, X. C. Du, W. S. Yang, L. H. Li, J. H. Hao and W. D. Shi, *J. Colloid Interface Sci.*, 2025, **681**, 261-268.

131. J. C. Ehlers, S. D. Egelund, G. O. Larrazábal and C. Chatzichristodoulou, *Chem. Eng. J*, 2025, **525**, 169990.

132. S. S. Kumar and H. Lim, *Energy Rep.*, 2022, **8**, 13793-13813.

133. H. Wakayama and K. Yamazaki, *Acs Omega*, 2021, **6**, 4161-4166.

134. P. Lettenmeier, R. Wang, R. Abouatallah, B. Saruhan, O. Freitag, P. Gazdzicki, T. Morawietz, R. Hiesgen, A. S. Gago and K. A. Friedrich, *Sci. Rep.*, 2017, **7**, 44035.

135. C. F. Wang, J. M. Stansberry, R. Mukundan, H. M. J. Chang, D. Kulkarni, A. M. Park, A. B. Plymill, N. M. Firas, C. P. Liu, J. T. Lang, J. K. Lee, N. E. Tolouei, Y. Morimoto, C. H. Wang, G. H. Zhu, J. Brouwer, P. Atanassov, C. B. Capuano, C. Mittelsteadt, X. Peng and I. V. Zenyuk, *Chem. Rev.*, 2025, **125**, 1257-1302.

136. S. Stiber, N. Sata, T. Morawietz, S. A. Ansar, T. Jahnke, J. K. Lee, A. Bazylak, A. Fallisch, A. S. Gago and K. A. Friedrich, *Energy Environ. Sci.*, 2022, **15**, 109-122.

137. Y. Y. Wang, W. Y. Wu, F. Chen, J. Huang, L. Qian, E. Placidi, W. D. Freitas, A. D'Epifanio, E. Traversae and J. Li, *Chem. Commun.*, 2025, **61**, 14446-14449.

138. M. M. Ikhsan, C. Y. Yang, K. Ghotia, F. Egert, S. A. Ansar, O. Zurowska, M. Rózga, A. Michalak, M. R. Kraglund, D. Aili, H. S. Park, F. Razmjooei and D. Henkensmeier, *Nat. Energy*, 2025, **10**, 1347-1359.

139. Z. C. Chen, L. Guo, L. Pan, T. Q. Yan, Z. X. He, Y. Li, C. X. Shi, Z. F. Huang, X. W. Zhang and J. J. Zou, *Adv. Energy Mater.*, 2022, **12**, 2103670.

140. K. X. Zhang, X. Liang, L. N. Wang, K. Sun, Y. N. Wang, Z. B. Xie, Q. N. Wu, X. Y. Bai, M. S. Hamdy, H. Chen and X. X. Zou, *Nano Res. Energy*, 2022, **1**, e9120032.

141. S. Stiber, H. Balzer, A. Wierhake, F. J. Wirkert, J. Roth, U. Rost, M. Brodmann, J. K. Lee, A. Bazylak, W. Waiblinger, A. S. Gago and K. A. Friedrich, *Adv. Energy Mater.*, 2021, **11**, 2100630.

142. Z. X. Qian, G. H. Liang, L. F. Shen, G. Zhang, S. S. Zheng, J. H. Tian, J. F. Li and H. Zhang, *J. Am. Chem. Soc.*, 2024, **147**, 1334-1343.

143. L. H. Zhang, Q. M. Bing, H. Qin, L. Yu, H. B. Li and D. H. Deng, *Matter*, 2025, **8**.

144. L. Wan, Z. Xu, Q. Xu, M. B. Pang, D. C. Lin, J. Liu and B. G. Wang, *Energy Environ. Sci.*, 2023, **16**, 1384-1430.

145. A. Prajapati, C. Hahn, I. M. Weidinger, Y. M. Shi, Y. H. Y. Lee, A. N. Alexandrova, D. Thompson, S. R. Bare, S. Chen, S. Yan and N. Kornienko, *Nat. Commun.*, 2025, **16**, 2593.

146. T. Hartman, R. G. Geitenbeek, C. S. Wondergem, W. van der Stam and B. M. Weckhuysen, *Acs Nano*, 2020, **14**, 3725-3735.

147. Y. G. Zhao, N. C. Dongfang, C. Huang, R. Erni, J. G. Li, H. Zhao, L. Pan, M. Iannuzzi and G. R. Patzke, *Nat. Commun.*, 2025, **16**, 580.

148. B. R. Cuenya and M. A. Banares, *Chem. Rev.*, 2024, **124**, 8011-8013.

149. L. K. Gao, X. Cui, C. D. Sewell, J. Li and Z. Q. Lin, *Chem. Soc. Rev.*, 2021, **50**, 8428-8469.

150. Y. M. Tian, P. F. Hou, Y. Y. Zhou and Q. Li, *J. Am. Chem. Soc.*, 2025, **147**, 35118-35127.

151. J. Abed, J. Heras-Domingo, R. Y. Sanspeur, M. C. Luo, W. Alnoush, D. M. Meira, H. T. Wang, J. Wang, J. G. Zhou, D. J. Zhou, K. Fatih, J. R. Kitchin, D. Higgins, Z. W. Ulissi and E. H. Sargent, *J. Am. Chem. Soc.*, 2024, **146**, 15740-15750.

152. S. D. Griesemer, Y. Xia and C. Wolverton, *Nat. Comput. Sci.*, 2023, **3**, 934-945.

153. N. Du, C. Roy, R. Peach, M. Turnbull, S. Thiele and C. Bock, *Chem. Rev.*, 2022, **122**, 11830-11895.

154. K. Li, S. L. Yu, D. G. Li, L. Ding, W. T. Wang, Z. Q. Xie, E. J. Park, C. Fujimoto, D. A. Cullen, Y. S. Kim and F. Y. Zhang, *ACS Appl. Mater.*, 2021, **13**, 50957-50964.

View Article Online
DOI: 10.1039/D6SC03869G

Data availability

No primary research results, software, or code have been included, and no new data were generated or analyzed as part of this review.